Cell

Structural basis of assembly and torque transmission of the bacterial flagellar motor

Graphical abstract

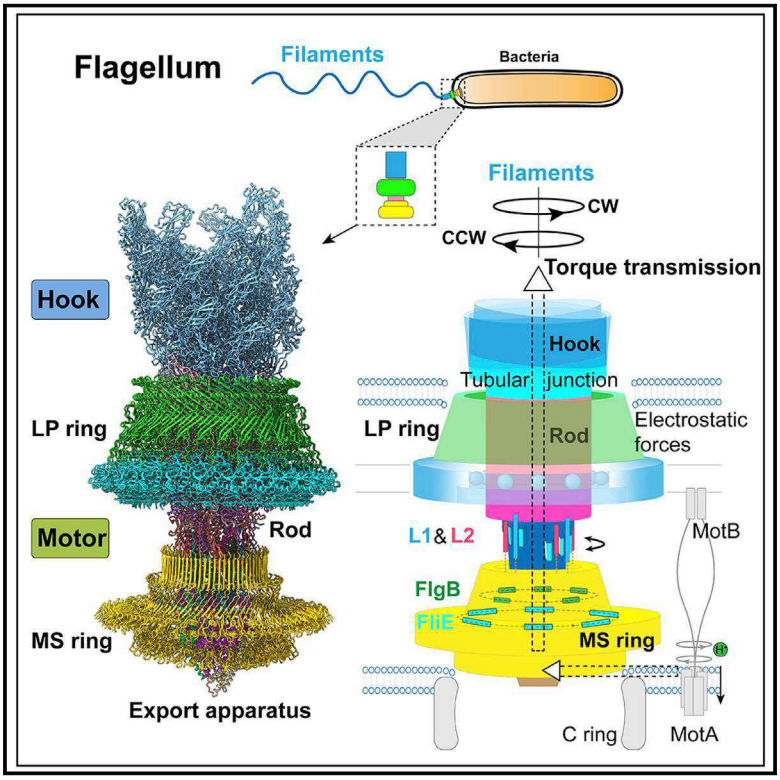

Highlights

- Cryo-EM structure of the bacterial flagellar motor complexed with the hook
- Each subunit in the rod interlocks with adjacent subunits
- Ten peptides, FlgB, and FliE are adaptors that join the MS ring and the rod
- The LP ring applies electrostatic forces to support rotation of the rod

Authors

Jiaxing Tan, Xing Zhang, Xiaofei Wang, ..., Haichun Gao, Yan Zhou, Yongqun Zhu

Correspondence

xzhang1999@zju.edu.cn (X.Z.), zhuyongqun@zju.edu.cn (Y. Zhu)

In brief

The cryo-EM structure of the *Salmonella* flagellar motor complexed with the hook reveals how the flagellar motor is assembled and carries out torque transmission to drive rotation of the flagellum.

Tan et al., 2021, Cell *184*, 1–15
May 13, 2021
https://doi.org/10.1016/j.cell.2021.03.057

CellPress

Please cite this article in press as: Tan et al., Structural basis of assembly and torque transmission of the bacterial flagellar motor, Cell (2021), https://doi.org/10.1016/j.cell.2021.03.057

Cell

CellPress

Article

Structural basis of assembly and torque transmission of the bacterial flagellar motor

Jiaxing Tan,[1,2,5,8] Xing Zhang,[1,4,6,8,*] Xiaofei Wang,[1,2,3,8] Caihuang Xu,[1,4,8] Shenghai Chang,[1,4] Hangjun Wu,[1,4] Ting Wang,[1,2,5] Huihui Liang,[5] Haichun Gao,[5] Yan Zhou,[1,2,5] and Yongqun Zhu[1,2,3,5,7,9,*]

[1]Department of Biophysics and Department of Pathology of Sir Run Run Shaw Hospital, Life Sciences Institute and School of Medicine, Zhejiang University, Hangzhou, Zhejiang 310058, China
[2]The MOE Key Laboratory for Biosystems Homeostasis & Protection and Zhejiang Provincial Key Laboratory of Cancer Molecular Cell Biology, Life Sciences Institute, Zhejiang University, Hangzhou, Zhejiang 310058, China
[3]The Second Affiliated Hospital, Zhejiang University School of Medicine, Hangzhou, Zhejiang 310058, China
[4]Center of Cryo Electron Microscopy, Zhejiang University, Hangzhou, Zhejiang 310058, China
[5]Institute of Microbiology, Zhejiang University, Hangzhou, Zhejiang 310058, China
[6]Liangzhu Laboratory, Zhejiang University Medical Center, Hangzhou, Zhejiang 311121, China
[7]Cancer Center, Zhejiang University, Hangzhou, Zhejiang 310058, China
[8]These authors contributed equally
[9]Lead contact
*Correspondence: xzhang1999@zju.edu.cn (X.Z.), zhuyongqun@zju.edu.cn (Y. Zhu)
https://doi.org/10.1016/j.cell.2021.03.057

SUMMARY

The bacterial flagellar motor is a supramolecular protein machine that drives rotation of the flagellum for motility, which is essential for bacterial survival in different environments and a key determinant of pathogenicity. The detailed structure of the flagellar motor remains unknown. Here we present an atomic-resolution cryoelectron microscopy (cryo-EM) structure of the bacterial flagellar motor complexed with the hook, consisting of 175 subunits with a molecular mass of approximately 6.3 MDa. The structure reveals that 10 peptides protruding from the MS ring with the FlgB and FliE subunits mediate torque transmission from the MS ring to the rod and overcome the symmetry mismatch between the rotational and helical structures in the motor. The LP ring contacts the distal rod and applies electrostatic forces to support its rotation and torque transmission to the hook. This work provides detailed molecular insights into the structure, assembly, and torque transmission mechanisms of the flagellar motor.

INTRODUCTION

Bacterial swimming and swarming motility is required for bacterial survival in different environments and biofilm formation and plays a variety of roles in pathogenesis, including reaching the optimal host site and invasion (Moens and Vanderleyden, 1996; Subramanian and Kearns, 2019). The bacterial flagellum is a huge protein machinery for bacterial swimming and swarming and is composed of about 25 different proteins, including structural and regulatory components (Armitage and Berry, 2020; Subramanian and Kearns, 2019; Takekawa et al., 2020). The structure of the flagellum consists of three distinct parts: a rotary motor, a universal joint, and a helical propeller (Berg, 2003; Carroll and Liu, 2020; Sowa and Berry, 2008). The rotary motor is powered by an ion-conducting stator, MotAB or PomAB, and is the assembly base of the flagellum (Deme et al., 2020; Santiveri et al., 2020). It spans the cytoplasmic and outer membranes and consists of the L ring, P ring, MS ring, C ring, the rod, and the export apparatus. The universal joint is the hook connecting the motor to the filament, which functions as the propeller of the flagellum to propel the bacterial cell and confer motility (Nakamura and Minamino, 2019).

The flagellar motor has an export apparatus in the cytoplasm, similar to that of bacterial type III secretion systems (T3SSs), to translocate the flagellar proteins across bacterial membranes (Johnson et al., 2019; Kawamoto et al., 2013). It has been proposed that the bacterial flagellum is the evolutionary ancestor of T3SSs (Deng et al., 2017; Erhardt et al., 2010). Unlike the T3SS basal body, which is fixed in bacterial membranes, the MS ring, C ring, and rod of the flagellar motor rotate at high speeds when they function (Armitage and Berry, 2020; Magariyama et al., 1994). The rotary MS ring in the bacterial inner membrane is assembled by the protein FliF (Ueno et al., 1992). It has been found that the MS ring contains about 24–36 copies of FliF with mixed internal symmetries (Johnson et al., 2020; Thomas et al., 2006). The C ring, which acts as the switch complex of the flagellar motor for rotational direction switching, is formed by the proteins FliG, FliM, and FliN and interacts dynamically with the cytoplasmic side of the MS ring (Chang et al., 2020; Francis et al., 1992; Minamino et al., 2019). The rod is coaxial

Please cite this article in press as: Tan et al., Structural basis of assembly and torque transmission of the bacterial flagellar motor, Cell (2021), https://doi.org/10.1016/j.cell.2021.03.057

with the MS ring and the LP ring and is made up of subunits of FliE, FlgB, FlgC, FlgF, and FlgG (Homma et al., 1990b; Jones et al., 1990; Müller et al., 1992). The outer-membrane L ring and the periplasmic P ring are assembled by the proteins FlgH and FlgI, respectively (Jones et al., 1987, 1989; Schoenhals and Macnab, 1996).

Because of its complexity, the flagellar motor is a highly challenging topic for biochemistry and structural biology studies. Many advances regarding its function, low-resolution imaging analyses, and force generation by the stator MotAB/PomAB, have been made during the past few decades (Carroll and Liu, 2020; Deme et al., 2020; Santiveri et al., 2020). Biochemical analyses have provided predictions regarding the stoichiometry of the components of the flagellar motor (Jones et al., 1990; Sosinsky et al., 1992a; Thomas et al., 2006). However, the detailed structure and the assembly and torque transmission mechanisms of the flagellar motor are still obscure. In this study, we determined the atomic-resolution cryoelectron microscopy (cryo-EM) structure of the flagellar motor in complex with the hook in the assembled state from *Salmonella enterica* Typhimurium. This work provides high-resolution structural insights into the assembly and torque transmission mechanisms of the flagellar motor.

RESULTS

Overall structure of the flagellar motor-hook complex

To investigate the structure of the flagellar motor, we generated a mutant strain of the *S. enterica* Typhimurium LT2 strain with double deletion of the genes of the filament protein FliC and its cap protein FliD to avoid effects of the flagellar filaments on purification of the motor. The mutant strain of *S.* Typhimurium produced the motor and the hook normally but did not assemble the filament. We designed a mild purification procedure for the motor particles based on previous studies (Aizawa, 2017; Aizawa et al., 1985; Francis et al., 1994). The purified motor sample was highly stable in negative staining and cryo-EM analyses (Figures S1A–S1C). As expected, the intact hook was contained in the purified motor particles. Because of the dynamic interactions of the stator MotA/B and the C ring with the MS ring (Armitage and Berry, 2020), negative staining analysis revealed that the stator and the C ring were not included in the particles. The initial reconstruction of the cryo-EM imaging data by C1 symmetry generated an average 3.9-Å density map of the motor-hook complex with global refinement, a 3.7-Å density map of the rod with the export apparatus and partial hook regions along the rod axis, and a 4.5-Å density map of the MS ring with the surrounded proximal rod and the export apparatus with local refinements. Further local refinements improved the resolution of the LP ring to 2.8 Å with C26 symmetry; that of the MS ring to 3.6 Å with C34 symmetry; that of the hook to 3.4 Å that of the rod to 3.3 Å; and those of the distal rod, proximal rod, and export apparatus with FliE subunits to 3.2 Å, 3.2 Å, and 3.6 Å, respectively, with C1 symmetry (Figures S1D, S1E, and S2A; Table S1).

The final structural model of the flagellar motor-hook complex contains 175 subunits from 12 proteins, which include 26 FlgH subunits in the L ring; 26 FlgI subunits in the P ring; 6 FliE, 5 FlgB, 6 FlgC, 5 FlgF, and 24 FlgG subunits in the rod; 5 FliP, 1 FliR, and 4 FliQ subunits in the export apparatus; 34 FliF subunits in the MS ring; and 33 FlgE subunits in part of the hook (Figures 1A–1C). The whole structure of the motor-hook complex has a molecular weight of ~6.3 MDa with a height of 460 Å. The part of the hook is in a curved state in the complex and is bound to the distal rod. The L and P rings interact tightly with each other and form the barrel-shaped LP ring. The distal rod, composed of FlgF and FlgG subunits, is surrounded by the LP ring (Figures 1B and 1D). The proximal rod, consisting of FliE, FlgB, and FlgC subunits, is relatively thin and bound to the export apparatus (Figure 1B). The MS ring embraces the export apparatus and the FliE- and FlgB-containing part of the proximal rod (Figures 1B, 1E, and 1F). Density maps of the MS ring obtained in local refinement did not reveal a clear transmembrane region, resulting in lack of a model of the inner membrane-binding domain of the MS ring in the complex structure. The overall structure of the motor-hook complex is larger and more complex than the T3SS basal body structure (Hu et al., 2019; Worrall et al., 2016).

The LP ring structure

The LP ring consists of 26 mature FlgH protomers (residues C22–M232) and 26 mature FlgI protomers (residues E20–I365) (Figure 2A). The L ring adopts a double-layered β-barrel structure, whereas the P ring contains three subrings (Figure 2B). The FlgH protomer in the L ring has an oblique arrow-like shape and consists of a long N-terminal loop (L_N), six central β strands (β1–β6), and three α helices (α1–α3) (Figures 2D and 2E). Strands β1, β2, and β5 form the long, inclined, anti-parallel β sheet S1, whose oligomerization forms the inner β-barrel of the L ring. Strands β3, β4, and β6 constitute the relatively short β sheet S2, whose oligomerization forms the outer β-barrel of the L ring (Figure 2B). S1 and S2 interact with each other through hydrophobic interactions via their N-terminal parts (Figures 2E, S3A, and S3B). In FlgH oligomerization for the L ring, S1 interacts with the C-terminal regions, and the linking hairpins of the S2 sheets of the prior two FlgH subunits, whereas S2 binds to the middle regions of the S1 sheets of the next two FlgH subunits (Figures 2F and S3C). The crossed interprotomer interactions of S1 and S2 not only connect the FlgH subunits in the L ring but also stabilize packing of the inner β-barrel with the outer β-barrel.

On the outer surface of the L ring, the N-terminal part (residues C22–V44) of the L_N loop binds to the S2 sheets of the next two FlgH subunits and extends its N terminus upward to interact with the C-terminal α2 and α3 helices of the two FlgH subunits (Figure 2F). The C-terminal region (residues P45–D76) of the L_N loop functions as a hanger to bind four FlgI subunits of the P ring (Figures 2F and 2K). The outer membrane-binding region of the L ring is formed by the horizontally arrayed α1 and α3 helices (Figure 2F). The first residue of the L_N loop, Cys22, has been suggested to be modified by fatty acylation (Schoenhals and Macnab, 1996). Indeed, clear electron density for a fatty acyl group could be observed on Cys22 in the density map of the L ring (Figures 2E). The fatty acyl group is inserted into the hydrophobic gap between the α3 helices of the next two FlgH subunits, which fixes the N termini of the FlgH subunits into the bacterial outer membrane (Figures 2F and 2G). Consistent with

Please cite this article in press as: Tan et al., Structural basis of assembly and torque transmission of the bacterial flagellar motor, Cell (2021), https://doi.org/10.1016/j.cell.2021.03.057

CellPress

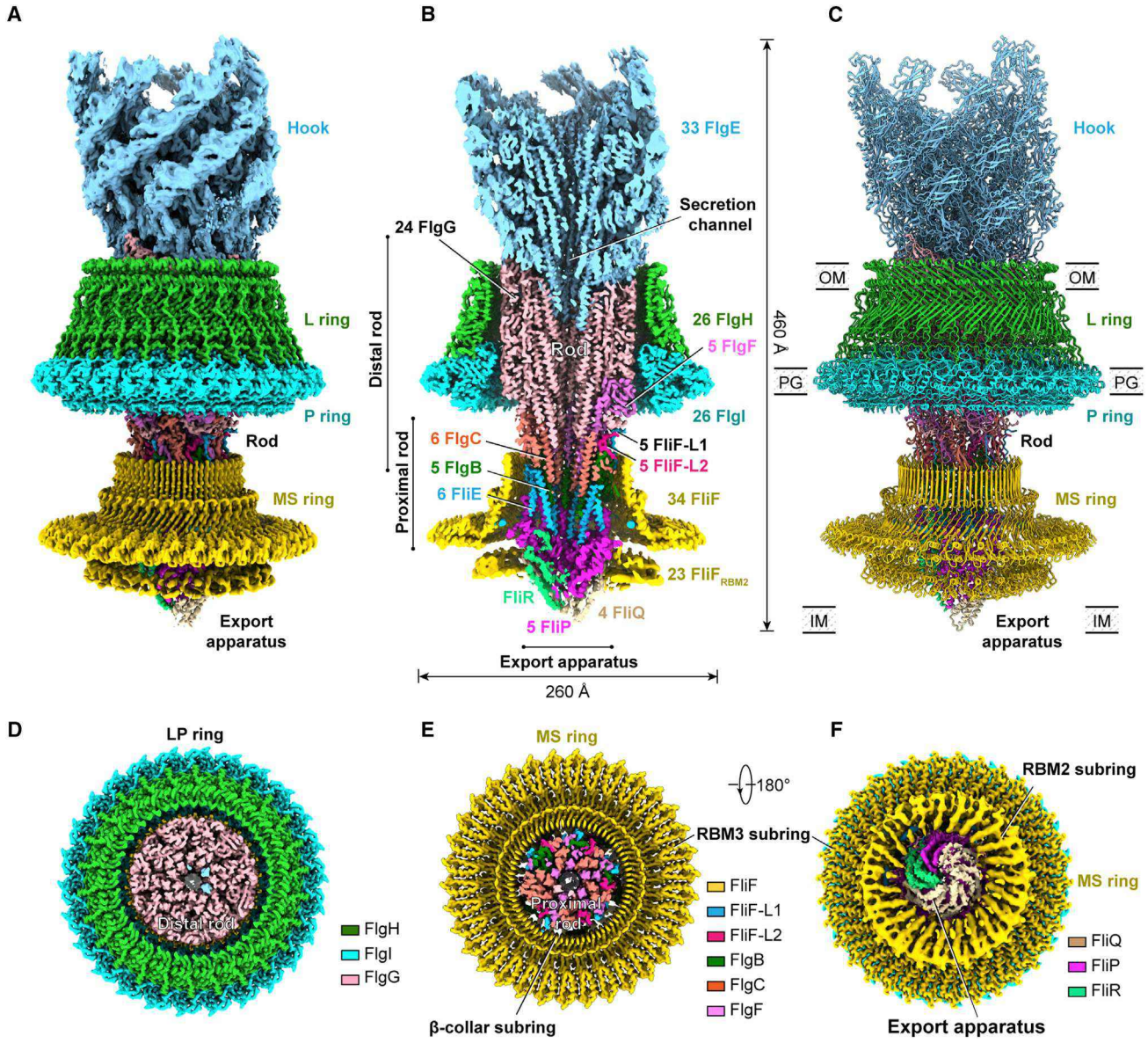

Figure 1. Overall structure of the flagellar motor-hook complex

(A) Merged density map of the flagellar motor-hook complex after local refinements. The map was obtained by fitting the high-resolution density maps of six locally refined regions (the LP ring, hook, rod, export apparatus, and the β-collar-RBM3 and RBM2 subrings of the MS ring) into the globally refined 3.9-Å-resolution map of the motor-hook complex.

(B) Cross-section view of the merged density map of the motor-hook complex. The subunit numbers of the components are labeled.

(C) Overall structure of the flagellar motor-hook complex.

(D–F) Cross-section views of the L ring (D) and MS ring (E) and bottom view (F) of the merged density map of the motor-hook complex.

The hook and the L, P, and MS rings are colored light blue, green, cyan, and yellow, respectively. OM, outer membrane; IM, inner membrane; PG, peptidoglycan.

crucial roles in FlgH oligomerization for the L ring, deletion of the C-terminal helices and mutation of the residue Cys22 abolishes bacterial motility (Schoenhals and Macnab, 1996).

The FlgI protomer adopts a twisted "V" shape and consists of an N-terminal D1 domain and two C-terminal ring-building motif (RBM) domains, RBM1 and RBM2 (Figures 2H and 2I). The three domains of FlgI constitute the upper (D1), outer (RBM1) and bottom (RBM2) subrings, respectively, of the P ring (Figures 2B and 2J). The D1 domain contains a core small β-barrel subdomain, a relatively separated helix α2, and the protruding linking loops L2 and L3 (Figure 2I). The RBM1 and RBM2 domains adopt a conserved β-α fold that exists in the T3SS components PrgK, PrgH, and InvG for formation of periplasmic rings (Spreter et al., 2009). However, FlgI does not exhibit sequence similarity with these T3SS components, indicating separate but convergent evolution of FlgI and the T3SS components for periplasmic binding.

Please cite this article in press as: Tan et al., Structural basis of assembly and torque transmission of the bacterial flagellar motor, Cell (2021), https://doi.org/10.1016/j.cell.2021.03.057

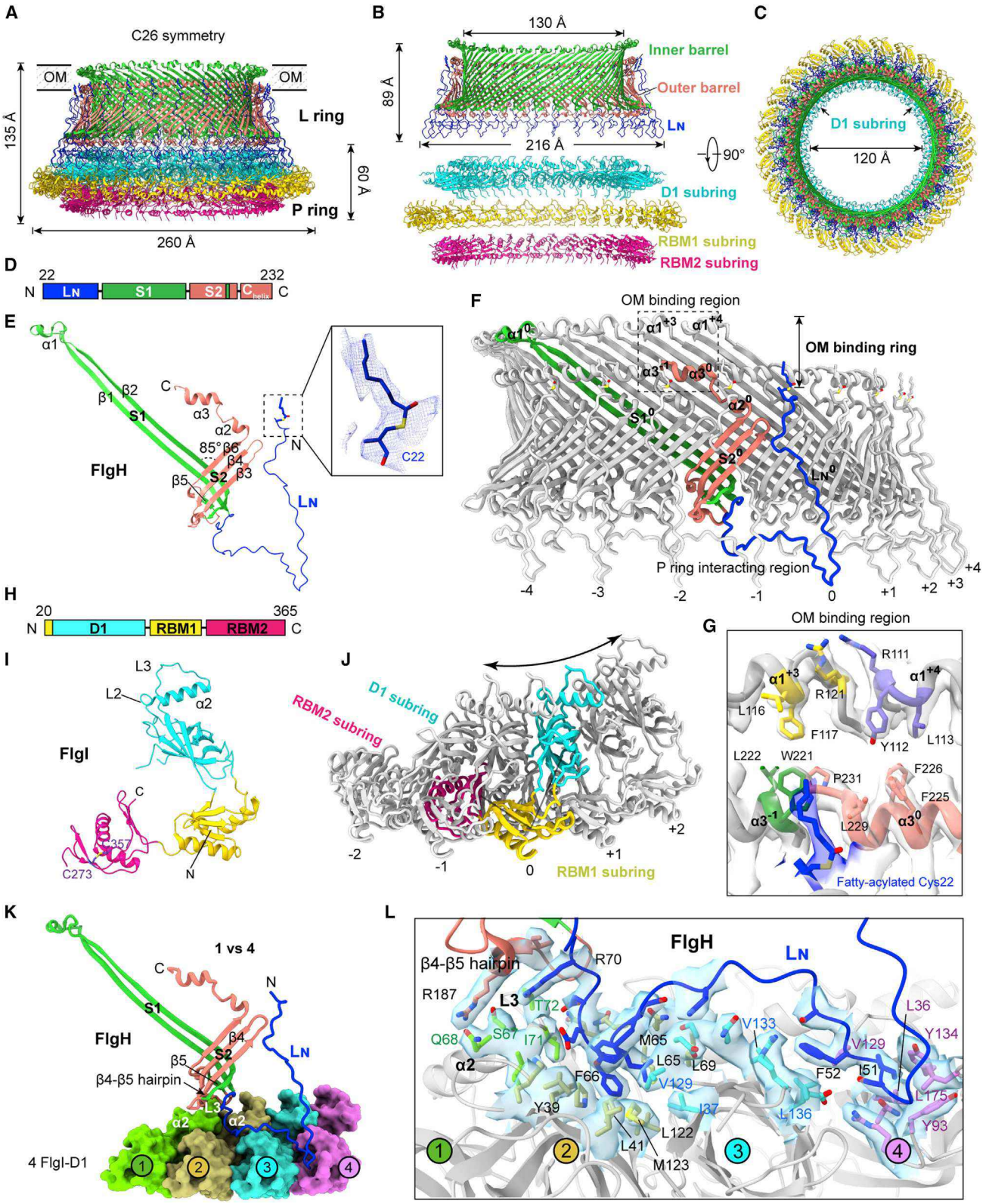

(legend on next page)

Please cite this article in press as: Tan et al., Structural basis of assembly and torque transmission of the bacterial flagellar motor, Cell (2021), https://doi.org/10.1016/j.cell.2021.03.057

During formation of the P ring, the D1 domain interacts extensively with neighboring D1 domains (Figures 2J and S3D), whereas the RBM1-RBM1 interfaces in the RBM1 subring are relatively small and rely mainly on interactions of the lateral α helices of RBM1 domains (Figure S3E). In the bottom RBM2 subring, the β1, β2, and β5 strands form a five-stranded antiparallel β sheet with β3 and β4 of the next RBM2 domain (Figure S3F). In turn, β3 and β4 of the RBM2 domain form an antiparallel β sheet with the β1, β2, and β5 strands of the prior RBM2 domain. This head-tail conjugation of the RBM2 domains results in tight assembly of the bottom RBM2 subring in the P ring. The D1 domain also forms cross-subring interactions with the RBM1 and RBM2 domains of the next FlgI subunits, which firmly connects the three subrings of the P ring (Figures S3G and S3H).

At the L-P interface, the FlgH and FlgI subunits interact with each other in a 1-versus-4 manner (Figure 2K). The C-terminal region of the L_N loop of FlgH binds sequentially to the D1 domains of four FlgI subunits (Figure 2L). The bottom hairpins of the S2 sheet of FlgH also interact with α2 and L3 of the prior FlgI subunit. In turn, a D1 domain in the P ring captures four L_N loops and one S2 sheet from four FlgH subunits of the L ring. The large interface between the L ring and the P ring indicates the high stability of the LP ring in the flagellar motor. Consistently, the intact LP ring complex could be observed even after disassembly of the flagellum (Kaplan et al., 2019b; Sosinsky et al., 1992b).

Sequence analysis revealed that the residues involved in oligomerization of FlgH and FlgI for formation of the LP ring are highly conserved, suggesting that assembly of FlgH and FlgI subunits for the LP ring is conserved across bacterial species (Figures S3I–S3K). However, the residues on the outer surface of the LP ring are highly variable in bacteria carrying the Na^+-driven flagellum, in which additional H and T rings are suggested to bind to the L ring and P ring, respectively, for fitness under harsh environmental conditions (Kaplan et al., 2019a; Minamino and Imada, 2015). The structure of the LP ring is significantly different from the C15-symmetric structure of the outer membrane-bound secretin of the bacterial T3SSs (Hu et al., 2019; Worrall et al., 2016; Figure S3L). The inclined S1 sheet of FlgH is much longer than the inner-barrel β sheet of secretin and results in a larger innermost diameter of the LP ring (Figure S3M).

The rod and its components

In the rod, the 6 FliE, 5 FlgB, 6 FlgC, 5 FlgF, and 24 FlgG subunits are packed sequentially from the proximal end to the distal end in a right-handed manner along the 1-start helical direction with helical parameters of ~4.3 Å and ~64.7° and are assembled into a prayer wheel shape for the rod (Figures 3A). The structure of the rod is divided into the thicker and double-layered tubular distal rod and the single-layered tubular proximal rod (Figure S4A).

The rod proteins harbor distinctive structural features (Figures 3B–3F and S4B–S4E). FliE is the simplest and consists of only three α helices: α1, α2, and α3 (Figure 3B). The N-terminal α1 is separated from the rod structure and binds to the inner surface of the MS ring (details are shown below). Helices α2 and α3 correspond to the α_N and α_C helices, respectively, of the D0 domains in other rod proteins (Figure S4C), although they do not contain any heptad repeats or the ANNLAN consensus sequence characteristic of the α_N and α_C helices (Homma et al., 1990a, 1990b; Müller et al., 1992). Among the 6 FliE subunits, the first subunit, $FliE^1$, lacks a clear density map of the α2 helix, probably because of special interactions with the FliR subunit of the export apparatus (Figure 3B). In addition to the D0 domain, the other rod proteins harbor a Dc domain (Figures 3C–3F). The FlgB Dc domain contains a unique α_B helix and extends a flexible loop region to interact with the MS ring (Figure 3C). The FlgC Dc domain contains a protruding loop (L_C) and a cap region that consists of a short β sheet and a long loop (Figures 3D). The featured structures of FlgC provide a molecular basis for its function as a transitional protein linking the proximal and distal rods. FlgF and FlgG have an additional D1 domain and adopt similar structures (Figures 3E, 3F, and S4E). FlgF has a characteristic loop (L6) and helix (α3) in its D1 domain, which results in the FlgF-containing part of the distal rod having a diameter larger than the inner diameter of the P ring, and precisely coordinates the position of the distal rod within the LP ring (Figures 1B and S4E). The Dc domain of FlgG is much longer than that of FlgF and contains a unique FlgG-specific sequence (GSS) region (residues Y46–P63) that consists of two antiparallel β strands with a long linking loop (Figures 3F, S4D, and S4E).

The intersubunit interactions for the high rigidity of the rod

Each subunit in the rod forms extensive interactions and interlocks with adjacent subunits (Figure 3A). In the inner D0 tube, hydrophobic interactions mediate stacking of the D0 domain with all six neighboring D0 domains (Figure S5A). Although FliE does not show sequence similarities to the D0 domains, the hydrophobic residues in the α2 and α3 helices mimic the heptad repeat to interact with the D0 domains of the FlgB and FlgC subunits. The N-terminal α_N helices of the rod proteins are longer than that of FlgE (Figure S5B). Along the 11-start helical direction, the α_N helix of a subunit directly contacts the α_C helix of

Figure 2. Structure of the LP ring and its assembly

(A) Overall structure of the LP ring.
(B) Separated cross-section view of the components of the L ring and the P ring.
(C) Top view of the LP ring.
(D and E) The domains (D) and structure (E) of FlgH. The density of the fatty acylated C22 residue is shown as blue mesh (right).
(F) The interprotomer interactions of FlgH in the L ring. Neighboring FlgH subunits are colored gray and numbered sequentially.
(G) Detailed interactions of α3 with the α1 helices of neighboring FlgH subunits in the L ring. The interacting residues and the fatty acylated C22 residue are shown as sticks with densities.
(H and I) The domains (H) and structure (I) of FlgI.
(J) The interprotomer interactions of FlgI in the P ring.
(K) The L-P interface. The four FlgI subunits bound by a FlgH subunit are colored green, gold, cyan, and purple, respectively.
(L) Detailed interactions of a FlgH subunit with the FlgI subunits of the P ring. The densities of the interacting residues of FlgH and FlgI are colored cyan.

Please cite this article in press as: Tan et al., Structural basis of assembly and torque transmission of the bacterial flagellar motor, Cell (2021), https://doi.org/10.1016/j.cell.2021.03.057

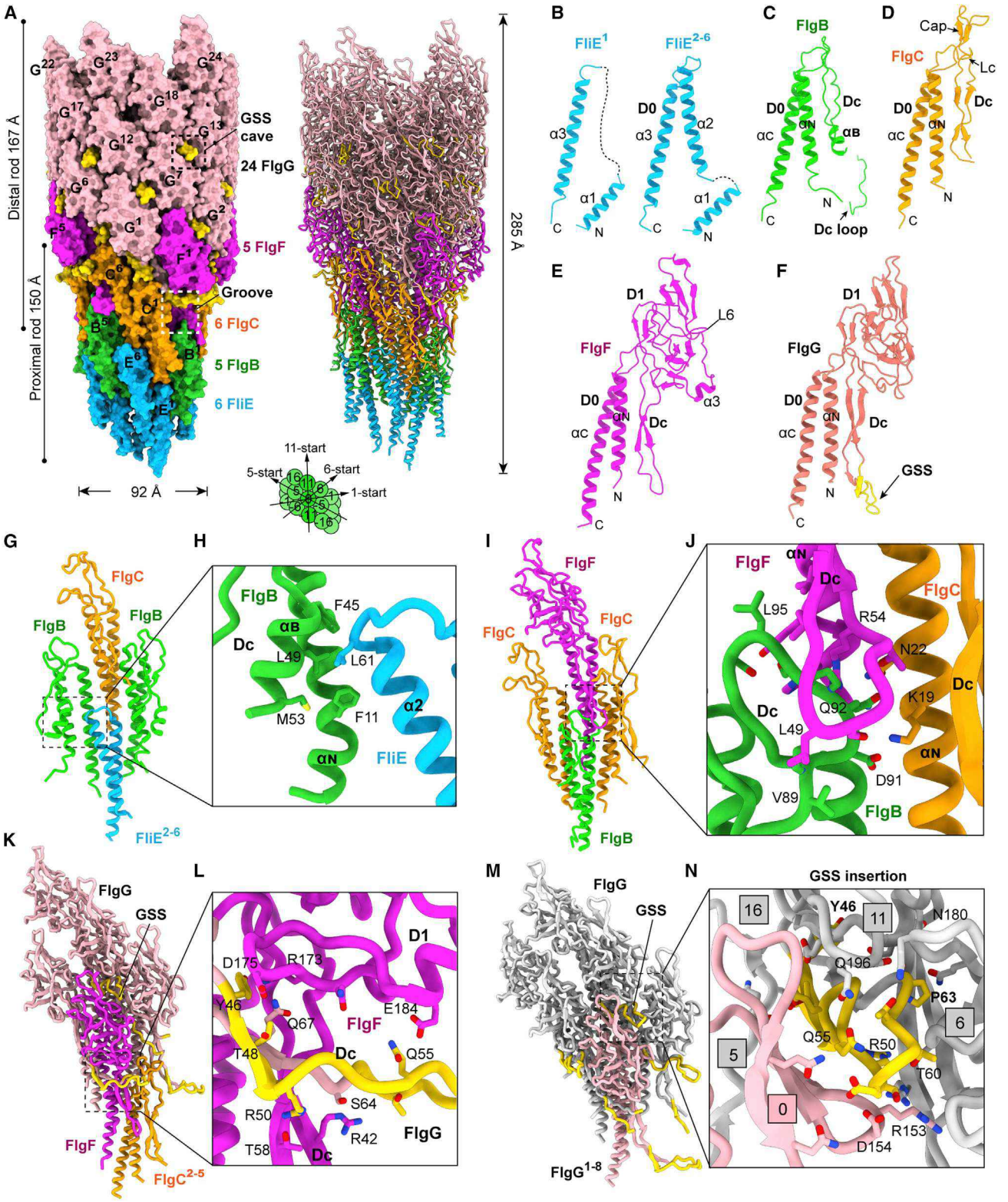

(legend on next page)

Please cite this article in press as: Tan et al., Structural basis of assembly and torque transmission of the bacterial flagellar motor, Cell (2021), https://doi.org/10.1016/j.cell.2021.03.057

the prior subunit (Figure S5C). Moreover, each D0 domain interacts with the Dc domains of the subunits along the 5- and −11-start helical directions, which strongly reinforces stacking of the D0 domains in the inner tube of the rod (Figures 3A and S5A). The head-to-tail interactions of the D0 domains and the Dc reinforcements result in the inner tube in the rod in the straight form.

In addition to the D0 domains, the Dc and D1 domains of the rod proteins build up extensive intersubunit interactions (Figure 3A). In the proximal rod, along the 5-start helical direction, the residues F45, L49, and M53 of the Dc domain of FlgB form strong hydrophobic stacking with F11 of the α_N helix of the FlgB D0 domain and Leu61 of FliE (Figures 3G, 3H, and S4F). Along the 11-start helical direction, the Dc domain of FlgF interacts with the upper loop region of the Dc domain of FlgB. Along the 6-start helical direction, the α_N helix of FlgC binds to the FlgB Dc domain to enhance the FlgB-FlgC interactions (Figures 3I, 3J, and S4G). In the distal rod, each FlgF subunit interacts with four FlgG subunits (Figure 3K). The D1 domains of the FlgF subunits interact with adjacent D1 domains of FlgG subunits along the 5-, 6-, and 11-start helical directions. The long Dc domain of the FlgG subunit at the 5-start position extends downward to embrace the D1 domain of the FlgF subunit and interacts with the cap region of the FlgC Dc domain, which not only ties the inner and outer tubes of the distal rod but also strengthens the connection of the distal rod with the proximal rod (Figures 3K, 3L, S4H, and S5D–S5H).

The FlgG GSS region is also involved in the intersubunit interactions in the distal rod and is crucial for maintaining its rigidity. On the outer surface of the distal rod, the interactions of a D1 domain of the FlgF or FlgG subunit with those of two neighboring FlgG subunits along the 11- and 6-start helical directions generate an open cave at the center (Figures 3A and S5I). The Dc domain of the FlgG subunit at the 16-start position inserts the unique GSS region as a wedge into the cave and stably interacts with the three D1 domains, which greatly strengthens the rigidity of the distal rod (Figures 3A, 3M, 3N, S4I, and S5J). Consistent with the importance of the GSS region in the rigidity of the distal rod, insertion of the GSS region into the corresponding region in the Dc domain of FlgE in the *Salmonella* genome made the hook of the bacteria straight and more rigid (Hiraoka et al., 2017). Because the Dc domain of FlgE is much shorter than that of FlgG (Figure S4E), the Dc domains of the FlgE subunits at the rod-hook interface cannot reach the 16 caves formed by the D1 domains of the $FlgG^{9–24}$ subunits along the 6-start directions and leave empty cavities on the distal rod surface (Figures 3A and S5I), suggesting that the upper and lower regions of the distal rod likely have different rigidities to enable torque transmission and the connection with the hook, respectively.

Molecular basis for torque transmission from the rod to the hook

The 3.4-Å-resolution map of the hook enabled us to build 33 FlgE subunits in the model (Figure S2A). The structure of the hook has a curved tubular architecture of three layers that are assembled by the D0, D1, and D2 domains of FlgE subunits, respectively (Figures S6A–S6E). At the rod-hook interface, 11 FlgE subunits ($FlgE^{1–11}$) interact directly with 11 FlgG subunits ($FlgG^{14–24}$) (Figures 4A–4C). The FlgE subunits insert their D0 domains into the inner tube of the distal rod, which forms stable $D0^{FlgE}$-$D0^{FlgG}$ hydrophobic stacking and connects the inner tube of the hook to that of the distal rod (Figures 4C and 4D). Packing of the FlgE and FlgG subunits along the 1-start helical direction at the interface results in each of the $FlgE^{1–5}$ subunits interacting with three FlgG subunits. $FlgE^{6}$ contacts two FlgG subunits ($FlgG^{19}$ and $FlgG^{24}$), whereas each of the $FlgE^{7-11}$ subunits interacts with one FlgG subunit (Figures 4E, S6F, and S6G). All D1 domains of the $FlgE^{1–11}$ subunits bind directly to adjacent D1 domains of FlgG subunits, generating a continuous $D1^{FlgG}$-$D1^{FlgE}$ domain interface and substantially connecting the middle tube of the hook with the outer tube of the distal rod (Figures 4B and 4F). The Dc domains of $FlgE^{1–11}$ subunits insert into the clefts underlying the D1 domains of FlgG and FlgE along the 6-start helical direction and interact with their D0, Dc, and D1 domains, which further strengthens the interactions of the inner and middle tubes of the hook with the distal rod (Figures 4E, 4G, S6F, and S6G). Thus, the extensive interactions of the D0, D1, and Dc domains of FlgE subunits with those of FlgG subunits at the rod-hook interface build up tight tubular junctions of the hook with the distal rod (Figures 4A and S5I), which ensures efficient torque transmission from the rod to the hook. In contrast, the D2 domain of FlgE, which is separated from its D1 domain, has no interaction with the rod and, therefore, is not involved in torque transmission (Figure 4B).

Structural basis of the export apparatus as the rod assembly base

The rod binds to the export apparatus via the FliE and FlgB subunits (Figure 5A). At the interface, the C-terminal regions

Figure 3. Structure of the rod and the intersubunit interactions

(A) Overall structure of the rod. The structure of the rod is represented in surface (left) and cartoon (right). The FliE, FlgB, FlgC, FlgF, and FlgG subunits are labeled as E, B, C, F, and G, respectively, with corresponding number superscripts. The helical directions for the rod assembly are indicated in the bottom green diagram.

(B–F) Structures of the rod proteins.

(G and H) Interactions of the $FliE^{2–6}$ subunits with FlgB and FlgC subunits in the rod. A magnified view of the interactions along the 5-start helical direction is shown in (H).

(I and J) Interactions of FlgB with FlgC and FlgF subunits in the rod. The interactions of the FlgB Dc domain with FlgC and FlgF subunits along the 6- and 11-start helical directions are shown in (J).

(K and L) Interactions of FlgF with the FlgC and FlgG subunits in the rod. Detailed interactions of the Dc domain of FlgG with the D1 domain of FlgF along the 5-start helical direction are shown in (L).

(M and N) Interactions of $FlgG^{1–8}$ with neighboring FlgG subunits in the distal rod. The interacting FlgG subunits are colored gray. Detailed interactions of the GSS region with the D1 domains of the FlgG subunits at the 0-, 5-, 6-, and 11-start positions, respectively, are shown in (N).

The GSS regions of FlgG subunits are highlighted in yellow (A, F, and K–N).

Please cite this article in press as: Tan et al., Structural basis of assembly and torque transmission of the bacterial flagellar motor, Cell (2021), https://doi.org/10.1016/j.cell.2021.03.057

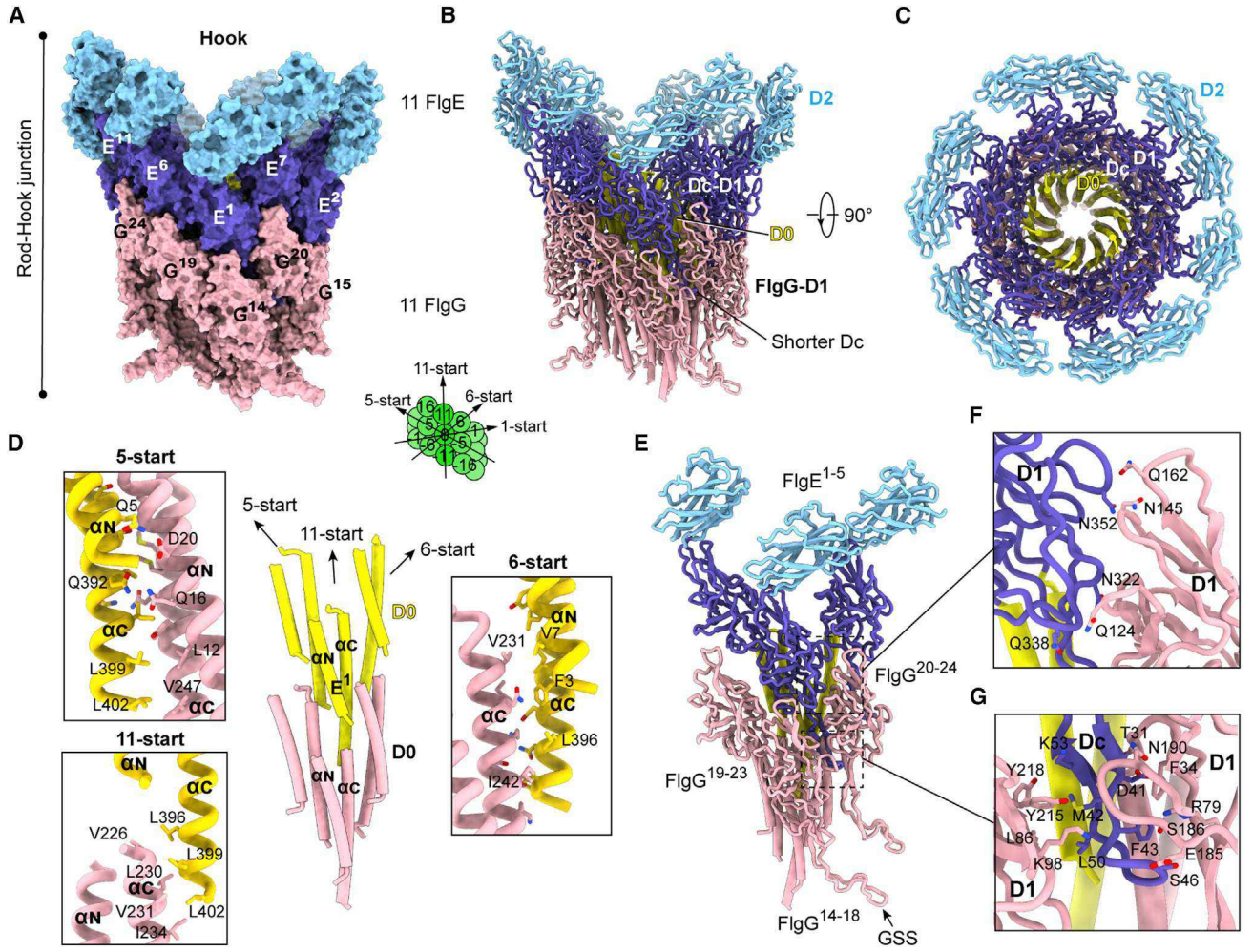

Figure 4. Interactions of the rod with the hook

(A and B) Surface representation (A) and cartoon illustration (B) of the rod-hook interface in the motor-hook complex. The FlgG and FlgE subunits are labeled briefly as G and E, respectively, with corresponding superscript numbers.

(C) Top view of the rod-hook interface in the motor-hook complex.

(D) Close-up view of the interactions of the FlgE^{1} D0 domain with neighboring FlgG D0 domains along the 5-, 6-, and 11-start helical directions at the rod-hook interface.

(E–G) Close-up view of the interactions of the Dc and D1 domains of FlgE with the FlgG subunits at the rod-hook interface. The representative interactions of FlgE$^{1–5}$ with FlgG subunits are illustrated (E). The detailed interactions of the FlgE D1 domain with that of FlgG along the 5-start helical direction and the interactions of the Dc domain of FlgE with FlgG subunits are illustrated in (F) and (G), respectively.

of the FliE α3 helices and the FlgB α_C helices are inserted obliquely into the lumen of the export apparatus. The N termini of the α2 helices of the FliE$^{2–5}$ subunits bind sequentially to the four grooves formed by the two neighboring subunits of FliP$^{1–5}$ (Figure 5A). The α2 helix of the FliE^{6} subunit is bound in the groove between FliR and the FliP^{5} subunit. In turn, the N-terminal helix bundles of the FliR and FliP subunits are embedded upward into the grooves between FliE and FlgB subunits (Figures 5A–5C). The interactions of the N-terminal α1 helices of the FliR and FliP subunits with the FliE α3 helices mimic the helical packing of the α_C helices in the inner D0 tube of the rod (Figures 5B–5D), suggesting that the FliR and FliP subunits of the export apparatus form the base for helical assembly of the inner tube of the rod.

In the FliE interactions with FliR and FliP, residues V99, M100, M102, and V104 in the α3 helices of the FliE subunits form strong hydrophobic interactions with the N-terminal helix hairpin 1 of FliR or FliP (Figure 5E). The αc helix and the N termini of the FlgB subunits interact with the N-terminal helices of the FliP subunits via hydrophobic and polar residues, including M130, V133, L134, L5, and R4 (Figure 5F). The interactions of the FliE^{1} α3 helix with FliR also mainly include hydrophobic interactions (Figure 5B). The extensive hydrophobic interactions of FliE and FlgB with the FliP and FliR subunits stably fix the proximal rod onto the export apparatus, suggesting that the export apparatus likely rotates together with the rod during motor functions. It has been suggested that FliE and FlgB are involved in activation of the export apparatus (Burrage et al., 2018; Zhao et al., 2013).

Please cite this article in press as: Tan et al., Structural basis of assembly and torque transmission of the bacterial flagellar motor, Cell (2021), https://doi.org/10.1016/j.cell.2021.03.057

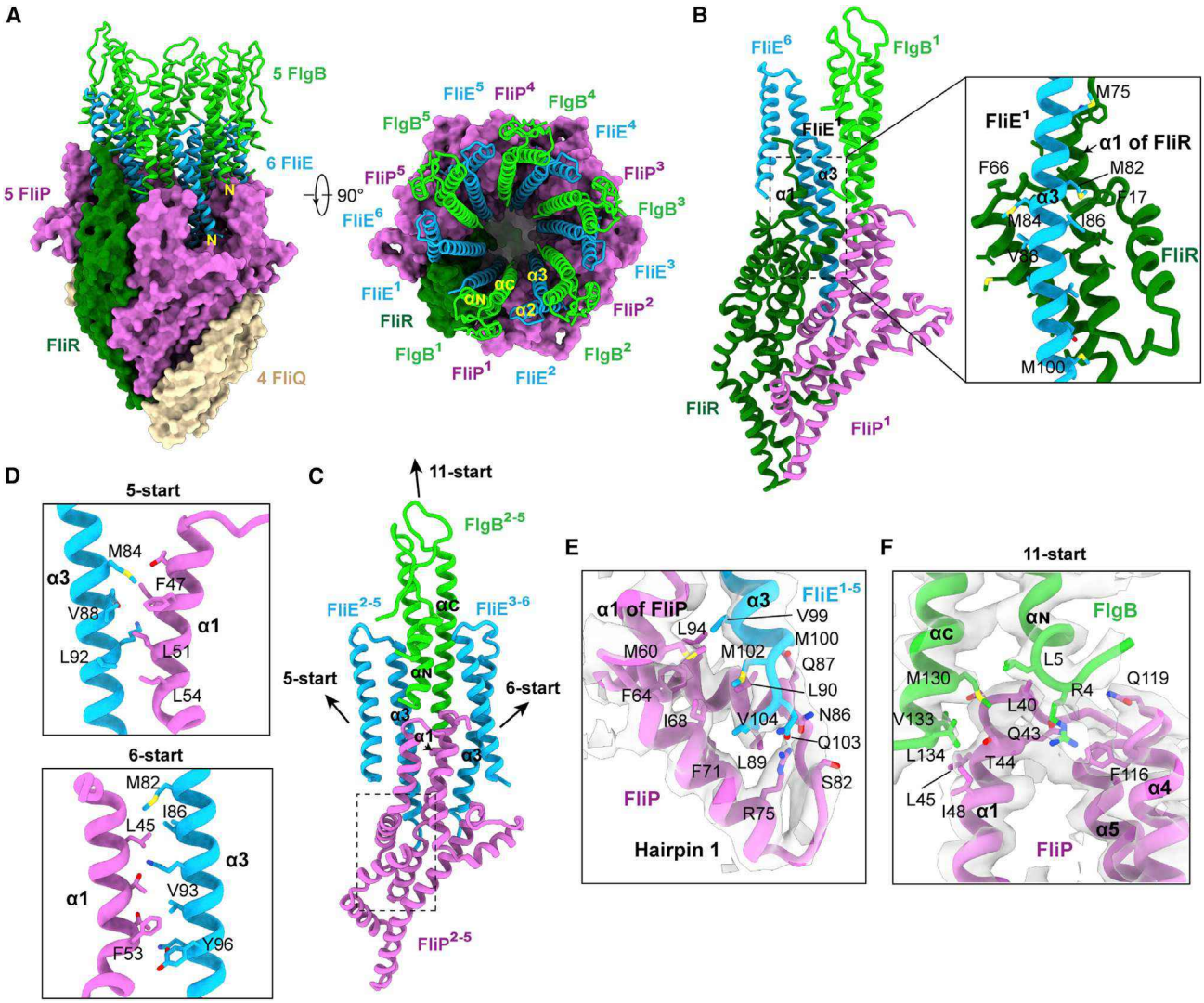

Figure 5. The interactions of the rod with the export apparatus

(A) Close-up view of the rod-export apparatus interface. The export apparatus is shown in surface. The FliE and FlgB subunits are shown in cartoon.

(B) Interactions of FliR with the FliE^1, FliE^6, FlgB^1, and FliP^1 subunits. A magnified view of the detailed interactions of FliR with the FliE^1 subunit is shown in the right box.

(C–F) Interactions of FliP with the FliE and FlgB subunits (C). Close-up views of the detailed interactions of the α1 helix of FliP with the α3 helices of the FliE subunits (D) along the 5- and 6-start directions, respectively, and the detailed interactions of hairpin 1 of FliP with the C terminus of FliE (E) and those of the N-terminal helices of FliP with FlgB along the 11-start helical direction (F) are shown. The interacting residues are shown as sticks with densities colored gray in (E) and (F).

Consistently, compared with the previously reported structure of the rod-free export apparatus (Kuhlen et al., 2018), binding of the FliE and FlgB subunits onto the export apparatus leads to outward movements of the N-terminal helices of FliP and FliR subunits by 13–30 Å (Figures S6H–S6J), respectively, and opens the channel of the export apparatus, suggesting that FliE and FlgB subunits activate and remodel the export apparatus to be a platform for assembly of the rod.

The LP ring-rod interface

How the LP ring facilitates rotation and torque transmission of the rod when the flagellum rotates at high speeds is unclear. The distal rod is accommodated coaxially within the LP ring (Figure 6A). The L ring has an inner diameter that is ~130 Å larger than the diameter of the distal rod, making no direct physical interactions with the FlgG-containing part of the distal rod (Figure 6B). Surface electrostatic potential analysis reveals that the top region of the inner surface of the L ring is fully charged with negative charges, which produce electrostatic repulsion to the distal rod that is also charged negatively for rotation. The middle and bottom regions of the inner surface of the L ring are charged positively and generate electrostatic attraction to the rod, which likely maintains the balance and coaxial orientation of the distal rod during its high-speed rotation (Figures 6C and 6D).

Please cite this article in press as: Tan et al., Structural basis of assembly and torque transmission of the bacterial flagellar motor, Cell (2021), https://doi.org/10.1016/j.cell.2021.03.057

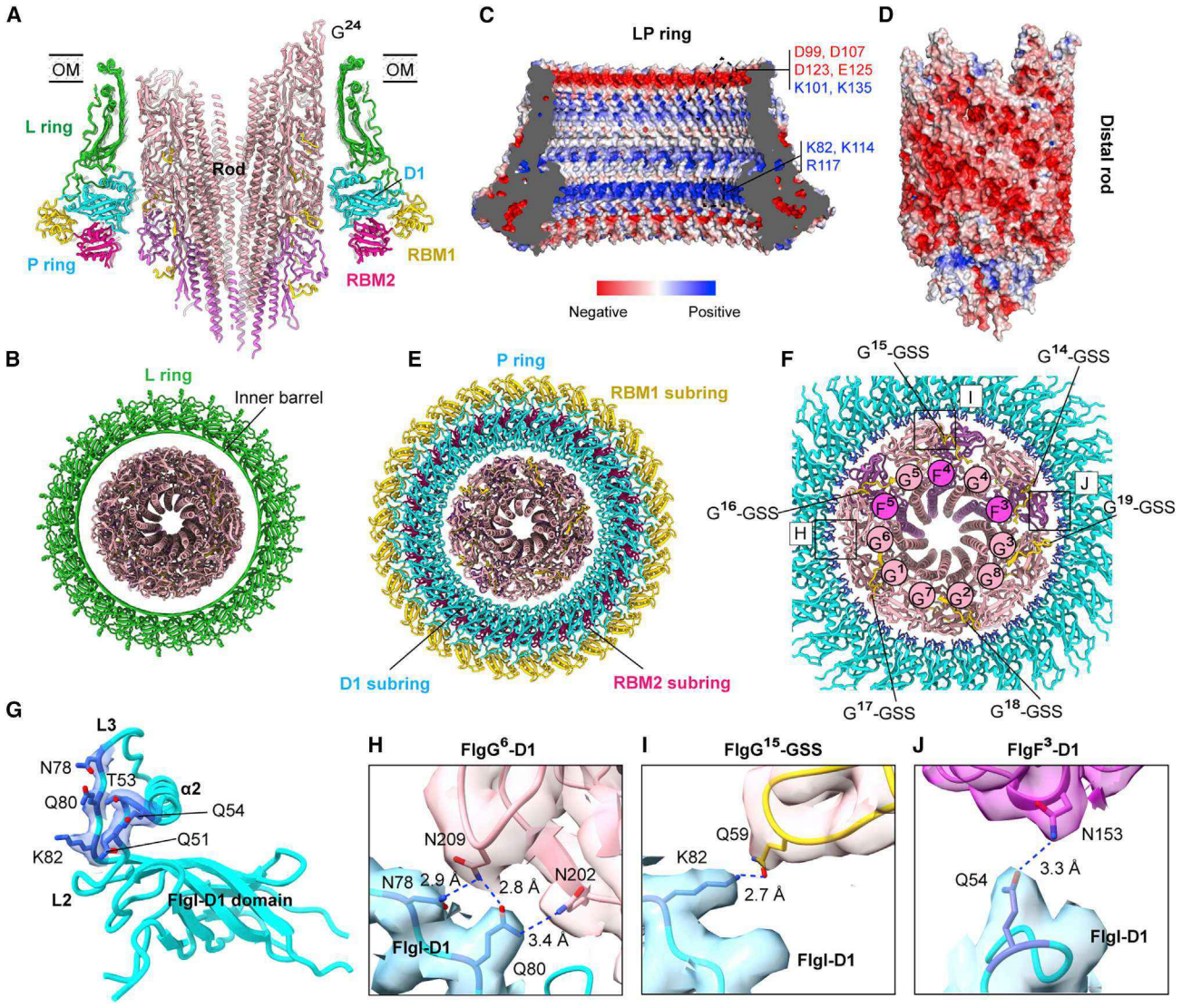

Figure 6. The interactions of the LP ring with the distal rod

(A) Cross-section view of the LP ring-rod interface.

(B) Top view of the distal rod within the L ring.

(C and D) The electrostatic potential distributions of the inner surface of the LP ring (C) and the outer surface of the distal rod (D). The surface is colored by relative electrostatic potential with red indicating negatively charged and blue positively charged.

(E) Top view of the interactions of the P ring with the distal rod.

(F) The interaction of the D1 subring of the P ring with the FlgF and FlgG subunits of the distal rod. The interacting residues of the P ring are shown as blue sticks.

(G) The rod-interacting residues in the D1 domain of FlgI.

(H–J) Close-up view of the detailed interactions of the D1 domains of the $FlgG^{6}$ and $FlgF^{3}$ subunits and the $FlgG^{15}$ GSS region with the D1 subring of the P ring. The densities of the interacting residues of the P ring and FlgG and FlgF subunits are colored cyan, salmon, and purple, respectively.

Unlike the L ring, the P ring interacts directly with the distal rod via the inner D1 subring (Figure 6E). The relatively separated α2 helix and the protruding L2 and L3 loops in the D1 domain of FlgI form the innermost edge of the P ring. The polar residues, including Q51, T53, Q54, N78, Q80, and K82, from the L2 and L3 loops on the inner surface of the D1 subring of the P ring interact with the $FlgF^{3–5}$, $FlgG^{1–8}$, and $FlgG^{14–19}$ subunits within distances of 2.6–3.5 Å (Figures 6F and 6G). The major P ring-interacting residues are asparagine, glutamine, glutamate, and aspartate, located in the D1 domains of the $FlgF^{3–5}$ and $FlgG^{1–8}$ subunits and in the GSS regions of the $FlgG^{14–19}$ subunits (Figures 6F and 6H–6J). The short distances of these hydrophilic residue-pair interactions indicate that the inner D1 subring of the P ring likely forms a hydrogen bond ring around the distal rod (Figures 6F). The hydrogen bonds formed by the invariant polar residues in the inner D1 subring of the P ring with the relatively invariant interacting residues of the FlgG and FlgF subunits allow the P ring to act as a ball bearing to stabilize the central

Please cite this article in press as: Tan et al., Structural basis of assembly and torque transmission of the bacterial flagellar motor, Cell (2021), https://doi.org/10.1016/j.cell.2021.03.057

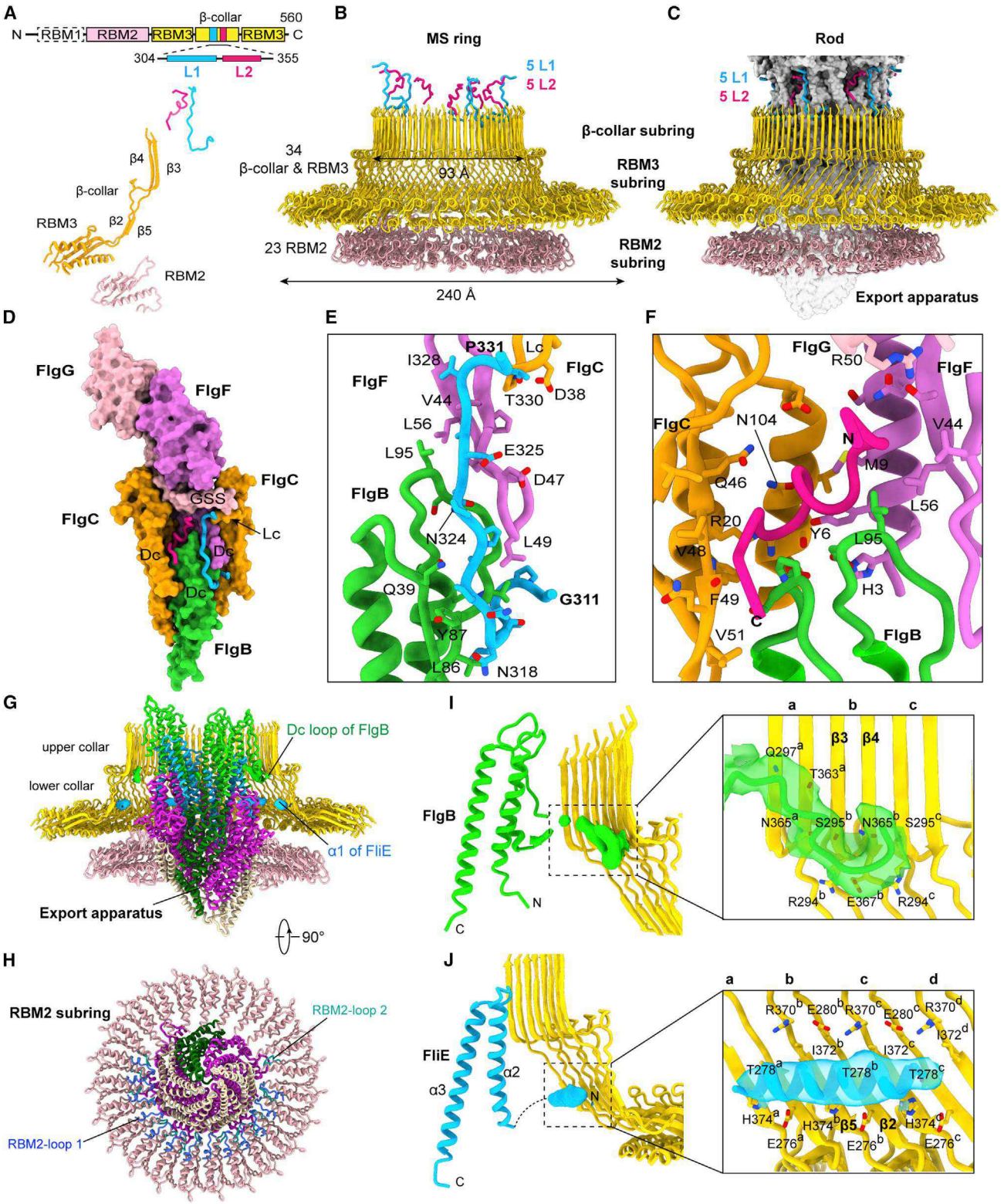

(legend on next page)

Please cite this article in press as: Tan et al., Structural basis of assembly and torque transmission of the bacterial flagellar motor, Cell (2021), https://doi.org/10.1016/j.cell.2021.03.057

localization of the rod in the P ring and enable rotation of the distal rod without significant structural obstacles or energy consumption. Thus, the LP ring applies electrostatic forces and a hydrogen bond ring to facilitate high-speed rotation and torque transmission of the rod.

The MS ring structure in the motor-hook complex

The 4.5-Å-resolution density map of the MS ring with the surrounded proximal rod and the export apparatus shows that the MS ring has significant mixed internal symmetries and is composed of 34 β-collar, 34 RBM3, and 23 RBM2 domains of FliF in the β-collar, RBM3, and bottom inner RBM2 subrings, respectively (Figures 7A, 7B, and S1D). Further refinements of the β-collar and RBM3 subrings with C34 symmetry improved their density map to a resolution of 3.6 Å (Figure S1D). The structure of a FliF protomer in the MS ring contains RBM2, RBM3, and β-collar domains but lacks the RBM1 domain and inner membrane-binding region because of the lack of density (Figure 7A). The MS ring forms a very large lumen to accommodate the export apparatus and the FliE- and FlgB-containing part of the proximal rod (Figures 1B and 7G). The ~98-Å diameter of the export apparatus is larger than the inner diameter of the upper β-collar subring, which prevents the export apparatus and the rod from dropping out from the MS ring (Figure 7B). The RBM2 subring also interacts with and stabilizes the export apparatus at the bottom side via the loop 1 and loop 2 regions (Figure 7H).

The MS ring-rod interactions and torque transmission

The MS ring not only functions as a structural component of the flagellar motor but is also responsible for torque transmission to the rod. In the motor-hook complex, the 3.2-Å-resolution density map of the proximal rod clearly reveals 5 pairs of L1 and L2 peptides, all of which are extended from the β-collar subring of the MS ring, bind to the outer surface of the proximal rod (Figures 7A–7C). The L1 peptides are bound into five shallow grooves formed by the upper regions of the FlgB Dc domains and the lower regions of the FlgF Dc domains with the L_C loops of FlgCs (Figure 7D). The residues of the L1 peptide (residues G311–P331) have been precisely identified in the map and are located in the flexible region that links the β3 and β4 strands of the β-collar domain of FliF (Figures 7A, 7B, and S7A). Each L1 peptide interacts with the FlgB, FlgC, and FlgF subunits through main-chain hydrogen bonds with hydrophobic contacts (Figures 7E and S7D). The five L1 peptides also interact with the inner surface of the β-collar subring via residues N318 and Q319 (Figures S7F and S7G).

Adjacent to the L1-binding grooves, the FlgB Dc domains also form 5 open pockets with adjacent FlgC, FlgG, and FlgF subunits that are packed along the 5-, 16-, and 11-start helical directions, respectively (Figure 7D). Each of the open pockets accommodates an L2 peptide. The densities of the L2 peptide allowed us to build 15 alanine residues for its model but limited precise determination of its sequence (Figure S7B). Given the distance of the C terminus of L2 to the MS ring, the L2 peptide likely contains the residues T^{333}NQQNAQNTPQTSTS^{347}, which are located in the C-terminal region of the flexible loop that links the β3 and β4 strands of FliF (Figure 7A). Like L1, the L2 peptide interacts with the rod mainly via main-chain hydrogen bonds with a few hydrophobic interactions (Figures 7F and S7E). The five pairs of L1 and L2 peptides are organized axially on the surface of the rod along the 1-start helical direction in a right-handed manner via the same axial helical parameters as those used by the rod proteins (Figures 7C and S7C). Given the short sequences between the L1 or L2 peptides with the β3 or β4 strands (Figure 7A), the long distance of ~23 Å between the N terminus of the L1 peptide and the C terminus of its neighboring L2 peptide (Figure S7H) suggests that a pair of adjacent L1 and L2 peptides are extended from two FliF subunits.

In addition to the L1- and L2-mediated MS ring-rod interactions, the 4.5-Å density map of the MS ring with the surrounded proximal rod and the export apparatus shows that a linking loop following the α_B helix in the Dc domain of each FlgB subunit (hereafter called the FlgB Dc loop) binds to the inner surface of the upper β3-β4 region of the β-collar subring of the MS ring (Figures 7G and 7I). The N-terminal α1 helices of the six FliE subunits of the proximal rod lie down and bind horizontally to the inner surface of the lower β2/β5 region of the β-collar subring (Figures 7G and 7J). The interface between the FlgB Dc loop and the β-collar subring covers three β3/β4 pairs of the MS ring and includes residues R294, S295, Q297, N365, and E367 of FliF (Figure 7I). The interactions of the FliE α1 helix with the MS ring cover four β2/β5 pairs. The hydrophobic and polar residues E276, T278, E280, R370, I372, and H374 are involved in the interactions (Figure 7J). Because of the low resolution, the MS ring-interacting residues in the FlgB Dc loop and FliE α1 helix were not determined. The interactions of FlgB and FliE subunits with the MS ring suggest that FlgB and FliE, not just FliE (Müller et al., 1992), are adaptors of the rod to the MS ring. The planar arrangements of the FlgB Dc

Figure 7. The interactions of the MS ring with the rod and the export apparatus

(A) Domain organization and structural model of a FliF protomer in the MS ring.

(B) Side view of the MS ring in the motor-hook complex.

(C) Interactions between the MS ring with the rod and export apparatus. The MS ring is represented in cartoon. The rod and export apparatus are shown as gray surfaces.

(D) Close-up view of the interactions of a pair of the L1 and L2 peptides with the rod.

(E and F) Detailed interactions of the L1 (E) and L2 (F) peptides with the rod proteins.

(G) Cross-section view of the interactions of the inner surface of the MS ring with the FlgB and FliE subunits and the export apparatus. The Dc loops of FlgBs and the α1 helices of FliEs are shown with densities.

(H) Bottom view of the interaction of the RBM2 subring with the export apparatus.

(I) Detailed interactions of the FlgB Dc loop with the MS ring.

(J) Detailed interactions of the FliE α1 helix with the MS ring.

The densities of the Dc loop of FlgB (I) and the α1 helix of FliE (J) are colored green and blue, respectively.

Please cite this article in press as: Tan et al., Structural basis of assembly and torque transmission of the bacterial flagellar motor, Cell (2021), https://doi.org/10.1016/j.cell.2021.03.057

linking loop and the FliE α1 helix regulate adaptation of the rod to the ring structure of the MS ring, whereas the axial distribution of the L1 and L2 peptides changes the rod-surrounding pattern of the MS ring to the axial rod-interacting pattern. Thus, the extensive interactions of the L1 and L2 peptides with the rod and those of the FlgB Dc linking loop and FliE α1 helix with the MS ring realize planar-to-axial torque transmission and overcome the mismatch between the rotational symmetry of the MS ring and the helical symmetry of the rod.

DISCUSSION

How the flagellar motor is assembled and carries out torque transmission is a long-standing question. Our structure reveals that the rod proteins make extensive intersubunit interactions via their distinctive structural elements and form a compacted structure with high rigidity for the rod to mediate torque reception from the MS ring and torque transmission to the hook. The LP ring-rod and MS ring-rod interactions subtly mediate rotation and torque transmission in the motor. The LP ring has been proposed to be assembled after formation of the rod (Chevance et al., 2007; Cohen et al., 2017; Cohen and Hughes, 2014). However, deletion of the *flgH* or *flgI* genes severely affected formation of the rod (Chevance et al., 2007; Cohen and Hughes, 2014; Minamino and Macnab, 1999; Suzuki and Komeda, 1981), which suggests that the LP ring is crucial for assembly of the rod. The interactions of the LP ring with the distal rod suggest that the LP ring assembly might be coupled with that of the distal rod.

Although the flagellum has been proposed to be the evolutionary ancestor of T3SSs, the structure of the flagellar motor is significantly different from that of the T3SS basal body (Figure S7I). The rod in the basal body of the *Salmonella* T3SS consists of two proteins, PrgJ and PrgI, and adopts a relatively simple helical structure. In contrast to the tight contacts of the T3SS rod with the secretin channel and the inner membrane ring, the flagellar rod has few contacts with the LP ring to facilitate its high-speed rotation and torque transmission. In addition, unlike the C24-symmetric inner membrane ring assembled by PrgH and PrgK in the *Salmonella* T3SS, the MS ring of the flagellar motor is composed of 34 FliF subunits with mixed internal symmetries. Therefore, the flagellar motor has evolved special structural elements for bacterial motility.

The flagellar motor is a rotary engine for torsional force transmission to enable bacterial motility. In contrast, the rotation of F/V-type ATPases, another type of natural rotational machinery (Kühlbrandt, 2019), transmits torque force to induce conformational changes of the enzymatic domain for ATP synthesis or hydrolysis. The torque transmission mechanism from the rotary ring structure to the axial rod in the flagellar motor (Figure S7J) is different from that utilized by F/V-ATPases, in which the membrane-bound rotary ring forms a perpendicular surface attachment with the central stalk via salt bridges for planar-to-axial torsional force transmission. Thus, this work presents the structural basis for assembly and torque transmission of the flagellar motor and indicates the diversity of torque transmission mechanisms of natural rotary protein machineries.

Limitations of the study

Although this study determined the structure of the motor-hook complex, there are some limitations. First, mutagenetic analyses of the interacting residues need to be performed *in vivo*. Second, the sequence of the L2 peptide of the MS ring needs to be verified experimentally. Finally, the structures of the C ring, the C ring-stator interface, and the MS-C ring interactions need to be investigated further.

STAR★METHODS

Detailed methods are provided in the online version of this paper and include the following:

- KEY RESOURCES TABLE
- RESOURCE AVAILABILITY
  - Lead contact
  - Materials availability
  - Data and code availability
- EXPERIMENTAL MODEL AND SUBJECT DETAILS
  - Bacterial strains and culture conditions
- METHOD DETAILS
  - Construction of the *Salmonella* Δ*fliCD* mutant strain
  - Purification of the motor-hook complex
  - Negative staining analysis
  - Cryo-EM data collection
  - Cryo-EM image processing
  - Model building and validation
- QUANTIFICATION AND STATISTICAL ANALYSIS

SUPPLEMENTAL INFORMATION

Supplemental information can be found online at https://doi.org/10.1016/j.cell.2021.03.057.

ACKNOWLEDGMENTS

This work was supported by the National Key Research and Development Program of China (2017YFA0504803 and 2018YFA0507700 to X.Z. and 2017YFA0503900 to Y. Zhu), NSFC (81925024 and 81530068 to Y. Zhu and 81501717 to Y. Zhou), Zhejiang NSF (R20H190001 to Y. Zhou), and the Fundamental Research Funds for the Central Universities of China. Y. Zhu was supported by the National High-level Talents Special Support Program.

AUTHOR CONTRIBUTIONS

Y. Zhu conceived the study. J.T., X.Z., and Y. Zhu designed the experiments. J.T. performed genetic deletion, purification, and model building and refinement. C.X. and J.T. collected the cryo-EM data. X.Z., X.W., and J.T. performed image processing and reconstructions. J.T. and S.C. built initial models. C.X. and H.W. participated in image processing. T.W., H.L., H.G., and Y. Zhou prepared reagents and provided assistance. J.T., X.Z., and Y. Zhu analyzed the data. Y. Zhu wrote the manuscript and supervised the study.

DECLARATION OF INTERESTS

The authors declare no competing interests.

Received: January 6, 2021
Revised: February 28, 2021
Accepted: March 29, 2021
Published: April 20, 2021

REFERENCES

Adams, P.D., Afonine, P.V., Bunkóczi, G., Chen, V.B., Davis, I.W., Echols, N., Headd, J.J., Hung, L.W., Kapral, G.J., Grosse-Kunstleve, R.W., et al. (2010). PHENIX: a comprehensive Python-based system for macromolecular structure solution. Acta Crystallogr. D Biol. Crystallogr. *66*, 213–221.

Afonine, P.V., Klaholz, B.P., Moriarty, N.W., Poon, B.K., Sobolev, O.V., Terwilliger, T.C., Adams, P.D., and Urzhumtsev, A. (2018). New tools for the analysis and validation of cryo-EM maps and atomic models. Acta Crystallogr. D Struct. Biol. *74*, 814–840.

Aizawa, S.-I. (2017). Purification and Characterization of the Bacterial Flagellar Basal Body from Salmonella enterica. In The Bacterial Flagellum, Methods in Molecular Biology, T. Minamino and K. Namba, eds. (Humana Press), pp. 87–96.

Aizawa, S.I., Dean, G.E., Jones, C.J., Macnab, R.M., and Yamaguchi, S. (1985). Purification and characterization of the flagellar hook-basal body complex of Salmonella typhimurium. J. Bacteriol. *161*, 836–849.

Armitage, J.P., and Berry, R.M. (2020). Assembly and Dynamics of the Bacterial Flagellum. Annu. Rev. Microbiol. *74*, 181–200.

Berg, H.C. (2003). The rotary motor of bacterial flagella. Annu. Rev. Biochem. *72*, 19–54.

Burrage, A.M., Vanderpool, E., and Kearns, D.B. (2018). Assembly Order of Flagellar Rod Subunits in Bacillus subtilis. J. Bacteriol. *200*, e00425-e18.

Carroll, B.L., and Liu, J. (2020). Structural Conservation and Adaptation of the Bacterial Flagella Motor. Biomolecules *10*, 1492.

Chang, Y., Zhang, K., Carroll, B.L., Zhao, X., Charon, N.W., Norris, S.J., Motaleb, M.A., Li, C., and Liu, J. (2020). Molecular mechanism for rotational switching of the bacterial flagellar motor. Nat. Struct. Mol. Biol. *27*, 1041–1047.

Chen, S., McMullan, G., Faruqi, A.R., Murshudov, G.N., Short, J.M., Scheres, S.H., and Henderson, R. (2013). High-resolution noise substitution to measure overfitting and validate resolution in 3D structure determination by single particle electron cryomicroscopy. Ultramicroscopy *135*, 24–35.

Chevance, F.F., Takahashi, N., Karlinsey, J.E., Gnerer, J., Hirano, T., Samudrala, R., Aizawa, S., and Hughes, K.T. (2007). The mechanism of outer membrane penetration by the eubacterial flagellum and implications for spirochete evolution. Genes Dev. *21*, 2326–2335.

Cohen, E.J., and Hughes, K.T. (2014). Rod-to-hook transition for extracellular flagellum assembly is catalyzed by the L-ring-dependent rod scaffold removal. J. Bacteriol. *196*, 2387–2395.

Cohen, E.J., Ferreira, J.L., Ladinsky, M.S., Beeby, M., and Hughes, K.T. (2017). Nanoscale-length control of the flagellar driveshaft requires hitting the tethered outer membrane. Science *356*, 197–200.

Deme, J.C., Johnson, S., Vickery, O., Aron, A., Monkhouse, H., Griffiths, T., James, R.H., Berks, B.C., Coulton, J.W., Stansfeld, P.J., and Lea, S.M. (2020). Structures of the stator complex that drives rotation of the bacterial flagellum. Nat. Microbiol. *5*, 1553–1564.

Deng, W., Marshall, N.C., Rowland, J.L., McCoy, J.M., Worrall, L.J., Santos, A.S., Strynadka, N.C.J., and Finlay, B.B. (2017). Assembly, structure, function and regulation of type III secretion systems. Nat. Rev. Microbiol. *15*, 323–337.

Emsley, P., Lohkamp, B., Scott, W.G., and Cowtan, K. (2010). Features and development of Coot. Acta Crystallogr. D Biol. Crystallogr. *66*, 486–501.

Erhardt, M., Namba, K., and Hughes, K.T. (2010). Bacterial nanomachines: the flagellum and type III injectisome. Cold Spring Harb. Perspect. Biol. *2*, a000299.

Francis, N.R., Irikura, V.M., Yamaguchi, S., DeRosier, D.J., and Macnab, R.M. (1992). Localization of the Salmonella typhimurium flagellar switch protein FliG to the cytoplasmic M-ring face of the basal body. Proc. Natl. Acad. Sci. USA *89*, 6304–6308.

Francis, N.R., Sosinsky, G.E., Thomas, D., and DeRosier, D.J. (1994). Isolation, characterization and structure of bacterial flagellar motors containing the switch complex. J. Mol. Biol. *235*, 1261–1270.

Fujii, T., Kato, T., Hiraoka, K.D., Miyata, T., Minamino, T., Chevance, F.F., Hughes, K.T., and Namba, K. (2017). Identical folds used for distinct mechanical functions of the bacterial flagellar rod and hook. Nat. Commun. *8*, 14276.

Goddard, T.D., Huang, C.C., Meng, E.C., Pettersen, E.F., Couch, G.S., Morris, J.H., and Ferrin, T.E. (2018). UCSF ChimeraX: Meeting modern challenges in visualization and analysis. Protein Sci. *27*, 14–25.

Hiraoka, K.D., Morimoto, Y.V., Inoue, Y., Fujii, T., Miyata, T., Makino, F., Minamino, T., and Namba, K. (2017). Straight and rigid flagellar hook made by insertion of the FlgG specific sequence into FlgE. Sci. Rep. *7*, 46723.

Homma, M., DeRosier, D.J., and Macnab, R.M. (1990a). Flagellar hook and hook-associated proteins of Salmonella typhimurium and their relationship to other axial components of the flagellum. J. Mol. Biol. *213*, 819–832.

Homma, M., Kutsukake, K., Hasebe, M., Iino, T., and Macnab, R.M. (1990b). FlgB, FlgC, FlgF and FlgG. A family of structurally related proteins in the flagellar basal body of Salmonella typhimurium. J. Mol. Biol. *211*, 465–477.

Hu, J., Worrall, L.J., Vuckovic, M., Hong, C., Deng, W., Atkinson, C.E., Brett Finlay, B., Yu, Z., and Strynadka, N.C.J. (2019). T3S injectisome needle complex structures in four distinct states reveal the basis of membrane coupling and assembly. Nat. Microbiol. *4*, 2010–2019.

Johnson, S., Kuhlen, L., Deme, J.C., Abrusci, P., and Lea, S.M. (2019). The Structure of an Injectisome Export Gate Demonstrates Conservation of Architecture in the Core Export Gate between Flagellar and Virulence Type III Secretion Systems. MBio *10*, e00818–e00819.

Johnson, S., Fong, Y.H., Deme, J.C., Furlong, E.J., Kuhlen, L., and Lea, S.M. (2020). Symmetry mismatch in the MS-ring of the bacterial flagellar rotor explains the structural coordination of secretion and rotation. Nat. Microbiol. *5*, 966–975.

Jones, C.J., Homma, M., and Macnab, R.M. (1987). Identification of proteins of the outer (L and P) rings of the flagellar basal body of Escherichia coli. J. Bacteriol. *169*, 1489–1492.

Jones, C.J., Homma, M., and Macnab, R.M. (1989). L-, P-, and M-ring proteins of the flagellar basal body of Salmonella typhimurium: gene sequences and deduced protein sequences. J. Bacteriol. *171*, 3890–3900.

Jones, C.J., Macnab, R.M., Okino, H., and Aizawa, S. (1990). Stoichiometric analysis of the flagellar hook-(basal-body) complex of Salmonella typhimurium. J. Mol. Biol. *212*, 377–387.

Kaplan, M., Ghosal, D., Subramanian, P., Oikonomou, C.M., Kjaer, A., Pirbadian, S., Ortega, D.R., Briegel, A., El-Naggar, M.Y., and Jensen, G.J. (2019a). The presence and absence of periplasmic rings in bacterial flagellar motors correlates with stator type. eLife *8*, e43487.

Kaplan, M., Subramanian, P., Ghosal, D., Oikonomou, C.M., Pirbadian, S., Starwalt-Lee, R., Mageswaran, S.K., Ortega, D.R., Gralnick, J.A., El-Naggar, M.Y., and Jensen, G.J. (2019b). In situ imaging of the bacterial flagellar motor disassembly and assembly processes. EMBO J. *38*, e100957.

Kawamoto, A., Morimoto, Y.V., Miyata, T., Minamino, T., Hughes, K.T., Kato, T., and Namba, K. (2013). Common and distinct structural features of Salmonella injectisome and flagellar basal body. Sci. Rep. *3*, 3369.

Kucukelbir, A., Sigworth, F.J., and Tagare, H.D. (2014). Quantifying the local resolution of cryo-EM density maps. Nat. Methods *11*, 63–65.

Kühlbrandt, W. (2019). Structure and Mechanisms of F-Type ATP Synthases. Annu. Rev. Biochem. *88*, 515–549.

Kuhlen, L., Abrusci, P., Johnson, S., Gault, J., Deme, J., Caesar, J., Dietsche, T., Mebrhatu, M.T., Ganief, T., Macek, B., et al. (2018). Structure of the core of the type III secretion system export apparatus. Nat. Struct. Mol. Biol. *25*, 583–590.

Magariyama, Y., Sugiyama, S., Muramoto, K., Maekawa, Y., Kawagishi, I., Imae, Y., and Kudo, S. (1994). Very fast flagellar rotation. Nature *371*, 752.

Mastronarde, D.N. (2005). Automated electron microscope tomography using robust prediction of specimen movements. J. Struct. Biol. *152*, 36–51.

Minamino, T., and Imada, K. (2015). The bacterial flagellar motor and its structural diversity. Trends Microbiol. *23*, 267–274.

Minamino, T., and Macnab, R.M. (1999). Components of the Salmonella flagellar export apparatus and classification of export substrates. J. Bacteriol. *181*, 1388–1394.

Minamino, T., Kinoshita, M., and Namba, K. (2019). Directional Switching Mechanism of the Bacterial Flagellar Motor. Comput. Struct. Biotechnol. J. *17*, 1075–1081.

Moens, S., and Vanderleyden, J. (1996). Functions of bacterial flagella. Crit. Rev. Microbiol. *22*, 67–100.

Müller, V., Jones, C.J., Kawagishi, I., Aizawa, S., and Macnab, R.M. (1992). Characterization of the fliE genes of Escherichia coli and Salmonella typhimurium and identification of the FliE protein as a component of the flagellar hook-basal body complex. J. Bacteriol. *174*, 2298–2304.

Nakamura, S., and Minamino, T. (2019). Flagella-Driven Motility of Bacteria. Biomolecules *9*, 279.

Pettersen, E.F., Goddard, T.D., Huang, C.C., Couch, G.S., Greenblatt, D.M., Meng, E.C., and Ferrin, T.E. (2004). UCSF Chimera–a visualization system for exploratory research and analysis. J. Comput. Chem. *25*, 1605–1612.

Punjani, A., Rubinstein, J.L., Fleet, D.J., and Brubaker, M.A. (2017). cryoSPARC: algorithms for rapid unsupervised cryo-EM structure determination. Nat. Methods *14*, 290–296.

Rosenthal, P.B., and Henderson, R. (2003). Optimal determination of particle orientation, absolute hand, and contrast loss in single-particle electron cryomicroscopy. J. Mol. Biol. *333*, 721–745.

Santiveri, M., Roa-Eguiara, A., Kühne, C., Wadhwa, N., Hu, H., Berg, H.C., Erhardt, M., and Taylor, N.M.I. (2020). Structure and Function of Stator Units of the Bacterial Flagellar Motor. Cell *183*, 244–257.e16.

Scheres, S.H. (2012). RELION: implementation of a Bayesian approach to cryo-EM structure determination. J. Struct. Biol. *180*, 519–530.

Schoenhals, G.J., and Macnab, R.M. (1996). Physiological and biochemical analyses of FlgH, a lipoprotein forming the outer membrane L ring of the flagellar basal body of Salmonella typhimurium. J. Bacteriol. *178*, 4200–4207.

Shibata, S., Matsunami, H., Aizawa, S.I., and Wolf, M. (2019). Torque transmission mechanism of the curved bacterial flagellar hook revealed by cryo-EM. Nat. Struct. Mol. Biol. *26*, 941–945.

Sosinsky, G.E., Francis, N.R., DeRosier, D.J., Wall, J.S., Simon, M.N., and Hainfeld, J. (1992a). Mass determination and estimation of subunit stoichiometry of the bacterial hook-basal body flagellar complex of Salmonella typhimurium by scanning transmission electron microscopy. Proc. Natl. Acad. Sci. USA *89*, 4801–4805.

Sosinsky, G.E., Francis, N.R., Stallmeyer, M.J., and DeRosier, D.J. (1992b). Substructure of the flagellar basal body of Salmonella typhimurium. J. Mol. Biol. *223*, 171–184.

Sowa, Y., and Berry, R.M. (2008). Bacterial flagellar motor. Q. Rev. Biophys. *41*, 103–132.

Spreter, T., Yip, C.K., Sanowar, S., André, I., Kimbrough, T.G., Vuckovic, M., Pfuetzner, R.A., Deng, W., Yu, A.C., Finlay, B.B., et al. (2009). A conserved structural motif mediates formation of the periplasmic rings in the type III secretion system. Nat. Struct. Mol. Biol. *16*, 468–476.

Subramanian, S., and Kearns, D.B. (2019). Functional Regulators of Bacterial Flagella. Annu. Rev. Microbiol. *73*, 225–246.

Suzuki, T., and Komeda, Y. (1981). Incomplete flagellar structures in Escherichia coli mutants. J. Bacteriol. *145*, 1036–1041.

Takekawa, N., Imada, K., and Homma, M. (2020). Structure and Energy-Conversion Mechanism of the Bacterial Na^+-Driven Flagellar Motor. Trends Microbiol. *28*, 719–731.

Thomas, D.R., Francis, N.R., Xu, C., and DeRosier, D.J. (2006). The three-dimensional structure of the flagellar rotor from a clockwise-locked mutant of Salmonella enterica serovar Typhimurium. J. Bacteriol. *188*, 7039–7048.

Ueno, T., Oosawa, K., and Aizawa, S. (1992). M ring, S ring and proximal rod of the flagellar basal body of Salmonella typhimurium are composed of subunits of a single protein, FliF. J. Mol. Biol. *227*, 672–677.

Williams, C.J., Headd, J.J., Moriarty, N.W., Prisant, M.G., Videau, L.L., Deis, L.N., Verma, V., Keedy, D.A., Hintze, B.J., Chen, V.B., et al. (2018). MolProbity: More and better reference data for improved all-atom structure validation. Protein Sci. *27*, 293–315.

Worrall, L.J., Hong, C., Vuckovic, M., Deng, W., Bergeron, J.R.C., Majewski, D.D., Huang, R.K., Spreter, T., Finlay, B.B., Yu, Z., and Strynadka, N.C.J. (2016). Near-atomic-resolution cryo-EM analysis of the Salmonella T3S injectisome basal body. Nature *540*, 597–601.

Zhao, X., Zhang, K., Boquoi, T., Hu, B., Motaleb, M.A., Miller, K.A., James, M.E., Charon, N.W., Manson, M.D., Norris, S.J., et al. (2013). Cryoelectron tomography reveals the sequential assembly of bacterial flagella in Borrelia burgdorferi. Proc. Natl. Acad. Sci. USA *110*, 14390–14395.

Zheng, S.Q., Palovcak, E., Armache, J.P., Verba, K.A., Cheng, Y., and Agard, D.A. (2017). MotionCor2: anisotropic correction of beam-induced motion for improved cryo-electron microscopy. Nat. Methods *14*, 331–332.

Please cite this article in press as: Tan et al., Structural basis of assembly and torque transmission of the bacterial flagellar motor, Cell (2021), https://doi.org/10.1016/j.cell.2021.03.057

STAR★METHODS

KEY RESOURCES TABLE

REAGENT or RESOURCE	SOURCE	IDENTIFIER
Bacterial and virus strains		
Salmonella enterica serovar Typhimurium LT2 strain	ATCC	ATCC 700720
Salmonella enterica serovar Typhimurium LT2 Δ*fliCD* strain	This paper	N/A
Escherichia coli SM10 λπ	This paper	N/A
Chemicals, peptides, and recombinant proteins		
Chloramphenicol	Sangon Biotech	Cat# A600118-0050
Streptomycin sulfate	Sangon Biotech	Cat# A610494-0050
Sucrose	Sangon Biotech	Cat# A502792-0500
Lysozyme	Sangon Biotech	Cat# A610308-0005
Triton X-100	Sangon Biotech	Cat# A600198-0500
n-Dodecyl-N,N-Dimethylamine-N-Oxide (LDAO)	Anatrace	Cat# D360
CsCl	Sangon Biotech	Cat# A620054-0250
Ethylenediaminetetraacetic acid (EDTA)	BBI Life Sciences	Cat# A600107-0500
Uranyl acetate (UA)	SPI-Chem	Cat# 02624-AB
Deposited data		
Coordinates and Cryo-EM map of the LP ring	This paper	PDB: 7CBL; EMDB: EMD-30335
Coordinates and Cryo-EM map of the whole rod (II)-FlgE	This paper	PDB: 7E82; EMDB: EMD-31008
Coordinates and Cryo-EM map of the whole rod (I)-export apparatus-FlgE	This paper	PDB: 7E80; EMDB: EMD-31006
Coordinates and Cryo-EM map of the MS ring (C34)	This paper	PDB: 7CG7; EMDB: EMD-30351
Coordinates and Cryo-EM map of the hook	This paper	PDB: 7CGB; EMDB: EMD-30354
Coordinates and Cryo-EM map of the distal rod-FlgE	This paper	PDB: 7CBM; EMDB: EMD-30336
Coordinates and Cryo-EM map of the proximal rod	This paper	PDB: 7CG0; EMDB: EMD-30348
Coordinates and Cryo-EM map of the export apparatus-FliE	This paper	PDB: 7CG4; EMDB: EMD-30350
Coordinates and Cryo-EM map of the MS ring (C1)-FliE-FlgB	This paper	PDB: 7E81; EMDB: EMD-31007
Coordinates and Cryo-EM map of the motor-hook	This paper	PDB: 7CGO; EMDB: EMD-30359
Recombinant DNA		
Plasmid: pDM4-Δ*fliCD*	This paper	N/A
Software and algorithms		
SerialEM	Mastronarde, 2005	https://bio3d.colorado.edu/SerialEM/
MotionCor2	Zheng et al., 2017	https://msg.ucsf.edu/
RELION	Scheres, 2012	https://www3.mrc-lmb.cam.ac.uk/relion/
cryoSPARC	Punjani et al., 2017	https://cryosparc.com/
UCSF PYEM	Daniel Asarnow, Yifan Cheng Lab	https://zenodo.org/record/3576630

(*Continued on next page*)

Please cite this article in press as: Tan et al., Structural basis of assembly and torque transmission of the bacterial flagellar motor, Cell (2021), https://doi.org/10.1016/j.cell.2021.03.057

Continued

REAGENT or RESOURCE	SOURCE	IDENTIFIER
UCSF Chimera	Pettersen et al., 2004	https://www.cgl.ucsf.edu/chimera/
UCSF ChimeraX	Goddard et al., 2018	https://www.cgl.ucsf.edu/chimerax/
Phenix	Adams et al., 2010	https://www.phenix-online.org/
Coot	Emsley et al., 2010	https://www2.mrc-lmb.cam.ac.uk/personal/pemsley/coot/
MolProbity	Williams et al., 2018	http://molprobity.biochem.duke.edu/
Pymol	The PyMOL Molecular Graphics System, Version 2.0 Schrödinger	https://pymol.org/2/
Illustrator	Adobe	N/A
Photoshop	Adobe	N/A
Graphpad prism 7.0	GraphPad	https://www.graphpad.com:443/
Other		
Dounce homogenizer	Wheaton	Cat# 357542
Quantifoil grid (Cu, 300 mesh, R1.2/1.3)	Quantifoil Micro Tools GMBH	Cat# Q38186
Superose 6 10/300 Increase GL	GE Healthcare Life Sciences	Cat# 29091596

RESOURCE AVAILABILITY

Lead contact

Further information and requests for resources and reagents should be directed to and will be fulfilled by the Lead Contact, Yongqun Zhu (zhuyongqun@zju.edu.cn).

Materials availability

Bacterial strains generated in this study are available upon request.

Data and code availability

The Cryo-EM density maps including the 3.9 Å-resolution map of the whole motor-hook complex, all high-resolution maps obtained by local refinements and all structural models have been deposited in the EMDB and PDB with the following accession numbers: the LP ring, EMDB: EMD-30335, PDB: 7CBL; the whole rod with a part of the hook, EMDB: EMD-31008, PDB: 7E82; the whole rod with the export apparatus, EMDB: EMD-31006, PDB: 7E80; the distal rod (including a part of the hook), EMDB: EMD-30336, PDB: 7CBM; the proximal rod, EMDB: EMD-30348 PDB: 7CG0; the export apparatus with FliE subunits, EMDB: EMD-30350, PDB: 7CG4; the MS ring (C34, β-collar-RBM3), EMDB: EMD-30351, PDB: 7CG7; the MS ring (C1, containing FliE, FlgB subunits and the export apparatus), EMDB: EMD-31007, PDB: 7E81; the hook, EMDB: EMD-30354, PDB: 7CGB; and the whole motor-hook complex, EMDB: EMD-30359, PDB: 7CGO.

EXPERIMENTAL MODEL AND SUBJECT DETAILS

Bacterial strains and culture conditions

Salmonella enterica serovar Typhimurium LT2 (ATCC 700720) WT and Δ*fliCD* strains were grown in 2YT or Luria-Bertani (LB) broth supplemented with streptomycin *(*10 μg/ml*)* at 37°C. *Escherichia coli* SM10 λπ was grown in 2YT medium.

METHOD DETAILS

Construction of the *Salmonella* Δ*fliCD* mutant strain

The in-frame deletion for both *fliC* and *fliD* genes in *Salmonella enterica* typhimurium LT2 strain was constructed by homologous recombination by using the pDM4 suicide vector. The DNA fragments containing 1000 basepairs of the upstream sequence of *fliC* and 1000 basepairs of the downstream sequence of *fliD* were ligated into the pDM4 vector. The ligated plasmid was then transformed into the donor *E. coli* SM10 λπ strain. The transformed *E. coli* SM10 λπ strain and the recipient wild-type *S*. enterica LT2 strain were cultured in 2YT medium at 37°C until the value of OD_{600} reached 0.6. The two strains were then mixed at a ratio of 1:1, and transferred onto a sterilized 0.22 μm membrane filter on 2YT agar plates without antibiotics at 30°C for mating overnight. Transconjugants were selected on 2YT agar plates containing 25 μg/ml chloramphenicol and 50 μg/ml streptomycin. The first recombinant colonies were confirmed by standard PCR with the 5′ and 3′ primers of sacB and fliFG genes, and grown on 2YT agar plates (without NaCl) supplemented with 6% sucrose in order to isolate the Δ*fliCD* mutant strains. Finally, the mutant strains were

Please cite this article in press as: Tan et al., Structural basis of assembly and torque transmission of the bacterial flagellar motor, Cell (2021), https://doi.org/10.1016/j.cell.2021.03.057

confirmed by standard PCR method using at least two different pairs of primers and further validated by DNA sequencing of the PCR products.

Purification of the motor-hook complex

The ΔfliCD strain was initially cultured in 5 mL 2YT liquid medium supplemented with streptomycin (10 μg/ml) at 37°C overnight. Then 1 mL of the cultured bacteria was transferred into 1 L LB broth supplemented with streptomycin. After grown for 6.5 h at 37°C, the cultured bacteria were harvested and resuspended in a buffer containing 100 mM Tris-HCl, pH 8.0, 10 mM EDTA, 500 mM sucrose and 0.1 mg/ml lysozyme, and incubated for 40 min on a shaker. Next, cells were further lysed by adding 1% (v/v) Triton X-100 and 10 mM $MgSO_4$ at 4°C for 10 min while stirring gently. The lysates were then added into the same volume of the mixed lysis buffer containing 100 mM Tris-HCl, pH 8.0, 10 mM EDTA, 500 mM sucrose, 0.1 mg/ml lysozyme, 1% (v/v) Triton X-100 and 10 mM $MgSO_4$, and further stirred in order to reduce the viscosity of the resulting solution. After incubation for 1 h, the cell debris were removed by the low-speed centrifugation at 14,000 rpm for 10 min. The pH value of the supernatant of the cell lysates was then adjusted to pH 11.0 by using 5 M NaOH stock solution. Denatured proteins in the cell lysates were next removed by the low-speed centrifugation at 14,000 rpm for 10 min. The supernatant was collected and subjected to high-speed centrifugation at 35,000 rpm for 1 h. After centrifugation, the pellets were harvested and resuspended in 50 mL of the buffer containing 100 mM KCl, 300 mM sucrose, and 0.1% Triton X-100 (pH 11.0, adjusted with 1M KOH) and homogenized gently with a Dounce homogenizer (7 mL Tissue Grinder, Dounce, #357542). The homogenates were gently mixed on a shaker for 1 h at 4°C for complete resuspension. After low-speed centrifugation at 14,000 rpm for 10 min, the supernatant of the homogenates was collected and subjected to high-speed centrifugation at 35,000 rpm for 1h in order to enrich the motor-hook complex particles in the pellets. The pellets were then resuspended in 4 mL of TET buffer containing 10 mM Tris-HCl, pH 8.0, 5 mM EDTA and 0.1% Triton X-100, and incubated for 1 h at 4°C. The CsCl powder (1.5 g) was subsequently added to the solution. Following addition of CsCl, the sample was diluted by adding the TET buffer to the final volume of 5 ml, and then loaded into the SW41 tubes for centrifugation at 25,000 rpm for 12 hours. The fractions containing the motor-hook complex at the bottom of the tubes were collected by drop collections (6 drops per tube) and validated by 15% SDS-PAGE with Coomassie blue staining. The samples were dialyzed for three times in the TET buffer at 4°C to remove CsCl in the solution. After dialysis, the motor-hook complex sample was collected (the dataset I) for cryo-EM analysis.

We also developed another method to purify the motor-hook complex. In brief, the detergent LDAO instead of Triton X-100 was added to the cell mixture at the final concentration of 1% (v/v) after the lysozyme digestion. The cell debris were removed by low-speed centrifugation at 14,000 rpm. After the following high-speed centrifugation *at* 40,000 rpm, the pellets were resuspended with the buffer containing 10 mM Tris-HCl, pH 8.0, 500 mM NaCl, 5 mM EDTA and 0.5% LDAO. The CsCl powder was then added to the sample. After centrifugation at the speed of 25,000 rpm for 16-18 h, the fractions containing the motor-hook complex were subjected to the Superose 6 10/300 GL column in the buffer containing 10 mM Tris-HCl, pH 8.0, 500 mM NaCl, 5 mM EDTA and 0.5% LDAO. The fractions of the motor-hook complex were collected for cryo-EM analysis of the dataset II.

Negative staining analysis

For negative staining, 3 μL of the motor-hook complex samples was loaded onto a glow-discharged carton grid (200 mesh) and stained with 2% Uranyl Acetate (UA). The prepared grids were examined using a transmission electron microscope operated at 120 kV (Tecnai G2 Spirit, FEI).

Cryo-EM data collection

For cryo-EM data collection, 2.5 μL of the motor-hook complex samples were loaded onto a glow-discharged Quantifoil carbon grid supported with graphene-oxide (300 mesh, R1.2/1.3). The samples were blotted by using an FEI Vitrobot at 100% humidity and 22°C for 6 s, and then submerged in liquid ethane by plunge-freezing. Cryo-EM images of the motor-hook complex were recorded on an FEI Titan Krios electron microscope operated at 300 kV with a nominal magnification of 22,500. Before data collection, the microscope was carefully aligned. Especially the coma-free alignment was performed to minimize the effects of beam tilt. Using serialEM software (Mastronarde, 2005), a total of 3,683 movies for the dataset I and 6,209 movies for the dataset II were recorded on a Gatan K2 summit camera at 4 frames/sec for 8 s with the super-resolution mode. The dose rate of the electron beam was set to ~10 e^-/s per physical pixel, resulting in a total electron dose of ~47 electrons/$Å^2$ on the specimen with the calibrated pixel size of 0.6535 Å/pixel at the super-resolution mode. The nominal defocus values were set from 1.3 to 1.8 μm.

Cryo-EM image processing

The drift correction and dose-weighting of all image stacks were performed with the MotionCor2 software (Zheng et al., 2017) to generate 2x binned images with a pixel size of 1.307 Å/pixel. Using RELION (Scheres, 2012), ~1,000 particles were manually picked, followed by a two-dimensional (2D) classification to generate a class average of the motor-hook complex as a template for particle auto-picking. Unless specified, all following image processing steps were performed with *cryoSPARC* (Punjani et al., 2017). The motion-corrected micrographs of the two datasets were individually imported into *cryoSPARC* (Punjani et al., 2017), and defocus values of the micrographs were accomplished.

The dataset I in which the MS ring is well preserved was selected to determine the density maps of the whole motor-hook complex and the MS ring. A total of 478,027 motor-hook complex particles were picked with a box size of 512 × 512 based on

Please cite this article in press as: Tan et al., Structural basis of assembly and torque transmission of the bacterial flagellar motor, Cell (2021), https://doi.org/10.1016/j.cell.2021.03.057

the template-picking. A subset of 61,875 particles was selected in 2D classification. A subset of 52,714 particles was produced in ab-initio 3D reconstruction and 3D hetero-refinements. After several rounds of 3D refinements, two rounds of CTF refinements and a round of local refinement with the mask of the whole motor-hook complex with C1 symmetry, an average 3.9 Å-resolution density map of the whole motor-hook complex was obtained. Local refinements of the MS ring with the embraced proximal rod and the export apparatus with C1 symmetry produced a 4.5 Å-resolution high-quality density map. Local refinements on the rod with the partial hook and the export apparatus along the rod axis produced a 3.7 Å-resolution density map. The density map of the MS ring clearly showed that the MS ring has a 34-fold symmetry in the β-collar and RBM3 subrings and a 23-fold symmetry in the bottom inner RBM2 subring. For further local refinements of the MS ring, 433,479 particles that were centered on the MS ring were picked with the 380 × 380 box size. The 2D classification resulted in a subset of 56,346 particles. After ab-initio 3D reconstruction, a subset of 45,830 particles was subjected to 3D hetero-refinements by C34 symmetry with the mask of the β-collar and RBM3 subrings, which improved the resolution of the MS ring to 3.6 Å.

We combined the cryo-EM datasets I and II for high-resolution local refinements of the LP ring, the part of the hook that binds to the distal rod, the rod and the export apparatus. 1,879,357 raw particles were automatically picked using template-based picking with a box size of 512 × 512. The local defocus and astigmatism values of each raw particle were determined. Initial particle screening using 2D classification resulted in 167,090 particles, and further screenings by three-dimensional 3D hetero-refinements produced 148,517 particles without a mask. The volume of the motor-hook complex was obtained using a subset of 102,044 particles and global refinement with C1 symmetry. To determine the symmetry of the LP ring, after 3D hetero-refinement, a subset of 38,414 particles was used to perform a C31 symmetry expansion using RELION (Scheres, 2012). Local refinements were performed on these symmetry-expanded data using a mask of the LP ring generated with *Chimera* (Pettersen et al., 2004). After four iterations of local refinements, the symmetry of the LP ring was eventually converged to the C26 symmetry with a resolution of 3.34 *Å*. Then the C26 symmetry was imposed to refine a dataset of 80,548 particles and generated a reconstruction at the resolution of 2.8 Å. For the hook (148,517 particles), the whole rod (102,044 particles), the distal rod (118,962 particles), the proximal rod (148,517 particles), and the export apparatus (148,517 particles), local refinements were performed with C1 symmetry and local masks at their corresponding positions. After several iterations of local refinements, the resolutions of the density maps of the hook, the whole rod, the distal rod, the proximal rod and the export apparatus in reconstructions reached the resolutions of 3.4 Å, 3.3 Å, 3.2 Å, 3.2 Å, and 3.6 Å, respectively. For symmetry expansion in RELION (Scheres, 2012), *cryoSPARC* parameter files were first converted to the RELION formation with the UCSF PYEM *(*https://zenodo.org/record/3576630*)*. All map sharpening were accomplished automatically within *cryoSPARC* (Punjani et al., 2017).

Model building and validation

The FlgH protomer (residues C22-M232) and the FlgI protomer (residues E20-I365) were built manually in the 2.8 Å-resolution density map of the LP ring in *Coot* (Emsley et al., 2010). The fatty-acylated residue Cys22 of FlgH was modeled as a S-Octanoyl-L-cysteine residue. The initial models of the FlgH and FlgI protomers were first refined individually in *Phenix* (Adams et al., 2010). The LP ring model was then built in *Chimera* (Pettersen et al., 2004) using C26 symmetry and the models of the FlgH and FlgI protomers, and refined in *Phenix* (Adams et al., 2010) with non-crystallographic symmetry (NCS) restraints.

The protomers of FlgF (residues D2-M250), FlgC (residues A2-Q134), FlgB (residues L2-G136), FliE (residues S33-V104), FliF-L1 (residues G311-P331) and FliF-L2 (modeled as 15 alanine residues) were built *de novo* in the 3.2 Å-resolution density maps of the distal rod and proximal rod in *Coot* (Emsley et al., 2010). The FlgG protomer was modeled based on the previously reported FlgG structural model (PDB: 6JZR) (Fujii et al., 2017). These protomers were individually refined in *Phenix* (Adams et al., 2010). The model of the whole rod was generated in *Chimera* (Pettersen et al., 2004) with the helical parameters: an axial rise of 4.3 Å and an azimuthal rotation of 64.7° (hereafter named as the axial parameters) by using the refined protomer structures of the rod proteins in the 3.3 Å-resolution density map of the rod. In total, 24 FlgG subunits, 5 FlgF subunits, 6 FlgC subunits, 5 FlgB subunits, 5 FliF L1 peptides, 5 FliF L2 peptides, and 6 FliE subunits were modeled in the structure. The structure of the hook protein FlgE was modeled based on the reported FlgE structural model (PDB: 6K3I) (Shibata et al., 2019). 33 FlgE subunits were modeled using the axial parameters in the 3.4 Å-density map of the hook in *Chimera* (Pettersen et al., 2004). The model of the proximal 11 FlgE subunits was carefully modeled within the 3.3 Å-resolution density map of the rod, and combined with the model of the rod for the refinement in *Phenix* (Adams et al., 2010). The other 22 FlgE subunits were modeled and refined in the 3.4 Å-resolution density map of the hook. The model of the export apparatus was built in its 3.6 Å-resolution density map according to the previously reported structure of the $FliP_5R_1Q_4$ complex ($FliP_5$-R_1Q_4, PDB: 6F2D) (Kuhlen et al., 2018). The model was first refined in *Phenix* (Adams et al., 2010) without NCS restraints. The models of the rod and the export apparatus were then fitted into in the 3.7 Å-resolution density map of the rod and and refined in *Phenix* (Adams et al., 2010) without NCS restraints.

The structure of the MS ring containing 34 FliF subunits was modeled by using the structures of the β-collar and RBM3 domains from the rod-free MS ring (PDB:6SCN) (Johnson et al., 2020) with C34 symmetry in the 3.6 Å-resolution density map of the MS ring obtained in local refinements. The model was refined in *Phenix* (Adams et al., 2010) with NCS restraints. The initial structural model of the inner RBM2 subring was manually built using the structural model of the RBM2 domain of the rod-free MS ring with C23 symmetry in the 4.5 Å-resolution density map of the MS ring in *Coot* (Emsley et al., 2010). The model of the inner RBM2 subring was refined in *Phenix* (Adams et al., 2010) without NCS restraints.

Please cite this article in press as: Tan et al., Structural basis of assembly and torque transmission of the bacterial flagellar motor, Cell (2021), https://doi.org/10.1016/j.cell.2021.03.057

The structural models of the LP ring, the hook, the rod with a part of the hook (3.3 Å), the rod with the export apparatus (3.7 Å), the MS ring (β-collar and RBM3 subrings) and the RBM2 subring of the MS ring were checked with *Molprobity* (Williams et al., 2018). The model of the whole motor-hook complex was built by merging these refined models in the 3.9 Å-resolution density map of the whole motor-hook complex. The positions of the LP ring and the MS ring in the motor-hook complex were accurately determined according to a locally refined map of the LP ring with the surrounded distal rod, the locally refined 4.5 Å-resolution map of the MS ring with the surrounded proximal rod and export apparatus, and the globally refined 3.9 Å-resolution map of the motor-hook complex. The structure of the motor-hook complex was checked with *Molprobity* (Williams et al., 2018). The statistics of the cryo-EM data collection, processing, model refinement and validation were listed in Table S1. All structural figures were prepared in UCSF *ChimeraX* (Goddard et al., 2018), *Chimera* (Pettersen et al., 2004), and PyMOL (https://pymol.org/2/).

QUANTIFICATION AND STATISTICAL ANALYSIS

In Figure S1 and Table S1, the tight and corrected Fourier Shell Correlation (FSC) curve raw data were calculated using a tight mask alone and a tight mask with correction by noise substitution, respectively, with two independent half-maps in *cryoSPARC* (Punjani et al., 2017), and illustrated with Graphpad prism 7.0 (https://www.graphpad.com:443/). The resolution estimations of cryo-EM density maps were based on the corrected FSC curves at the FSC = 0.143 criterion (Chen et al., 2013; Rosenthal and Henderson, 2003). The model resolutions were evaluated using phenix.mtriage (Afonine et al., 2018) with the model-based noise free and experimental maps at the FSC = 0.5 criterion. The local resolutions were determined using ResMap (Kucukelbir et al., 2014) with two independent half-maps.

Supplemental figures

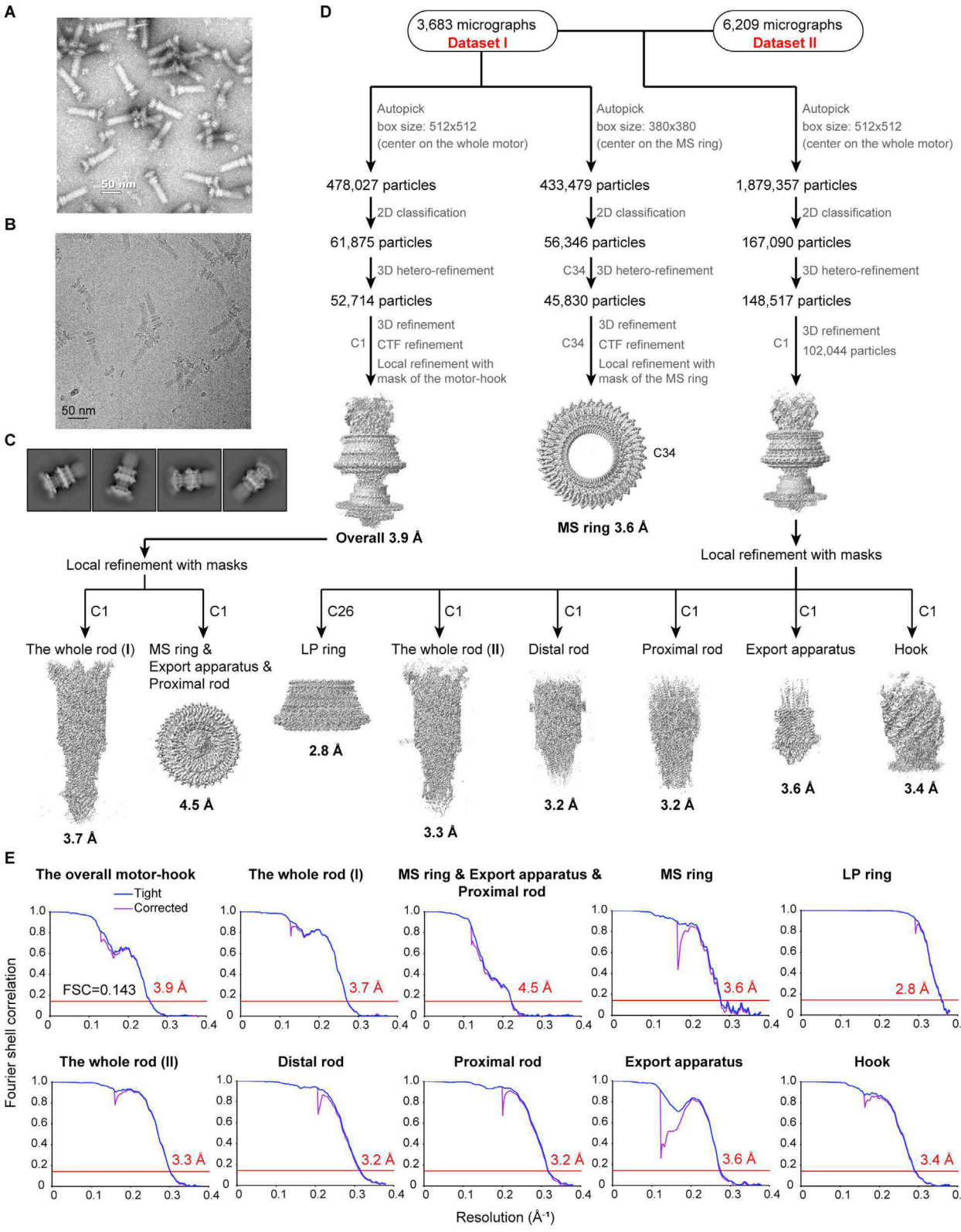

(legend on next page)

Figure S1. Negative staining and cryo-EM data processing of the motor-hook complex, related to Figure 1

(A) A representative negative-staining EM micrograph of the purified motor-hook complex in the buffer containing 10 mM Tris-HCl, pH 8.0, 5 mM EDTA, 0.1% Triton X-100, and 30% CsCl. High concentration of CsCl induced the hooks of some motor-hook particles in a straight state. Scale bar, 50 nm.

(B) A representative cryo-EM micrograph of the purified motor-hook complex collected on 300 kV. Scale bar, 50 nm.

(C) Representative 2D class averages for the dataset I of the particles of the motor-hook complex.

(D) The flow chart for the cryo-EM Data processing and structure determination of the motor-hook complex. Two datasets of cryo-EM data were collected for structure determination of the motor-hook complex. On the basis of the FSC value of 0.143, the reconstruction of the dataset I of cryo-EM images has an average resolution of 3.9 Å for the whole motor-hook complex. Local refinements along the rod axis produced a 3.7 Å-resolution density map for the rod with the export apparatus and a proximal part of the hook. Local refinements focusing on the MS ring with the surrounded proximal rod and the export apparatus with C1 symmetry produced a 4.5 Å-resolution density map and revealed 34 copies of FliF in the β-collar and RBM3 subrings of the MS ring and 23 copies of the RBM2 domain in the bottom RBM2 subring. Further local refinements with C34 symmetry for the upper β-collar and RBM3 subrings produced a 3.6 Å-resolution density map. Local refinements of the LP ring, the distal rod, the proximal rod, the export apparatus with FliE subunits, and the part of the hook that binds to the distal rod were performed using the combined data of the datasets I and II of images. All density maps were prepared using *ChimeraX*.

(E) The FSC curves for the reconstructions in (D).

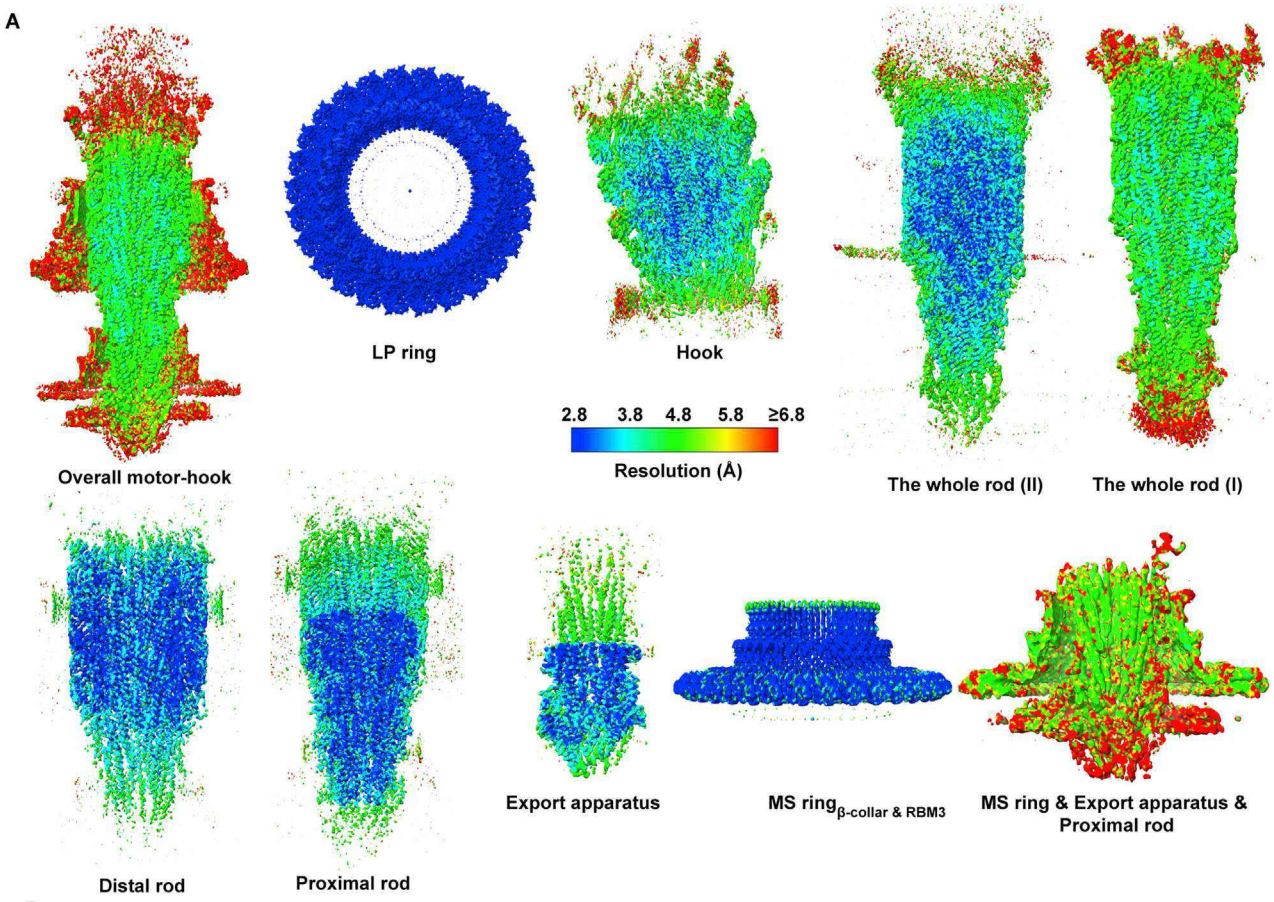

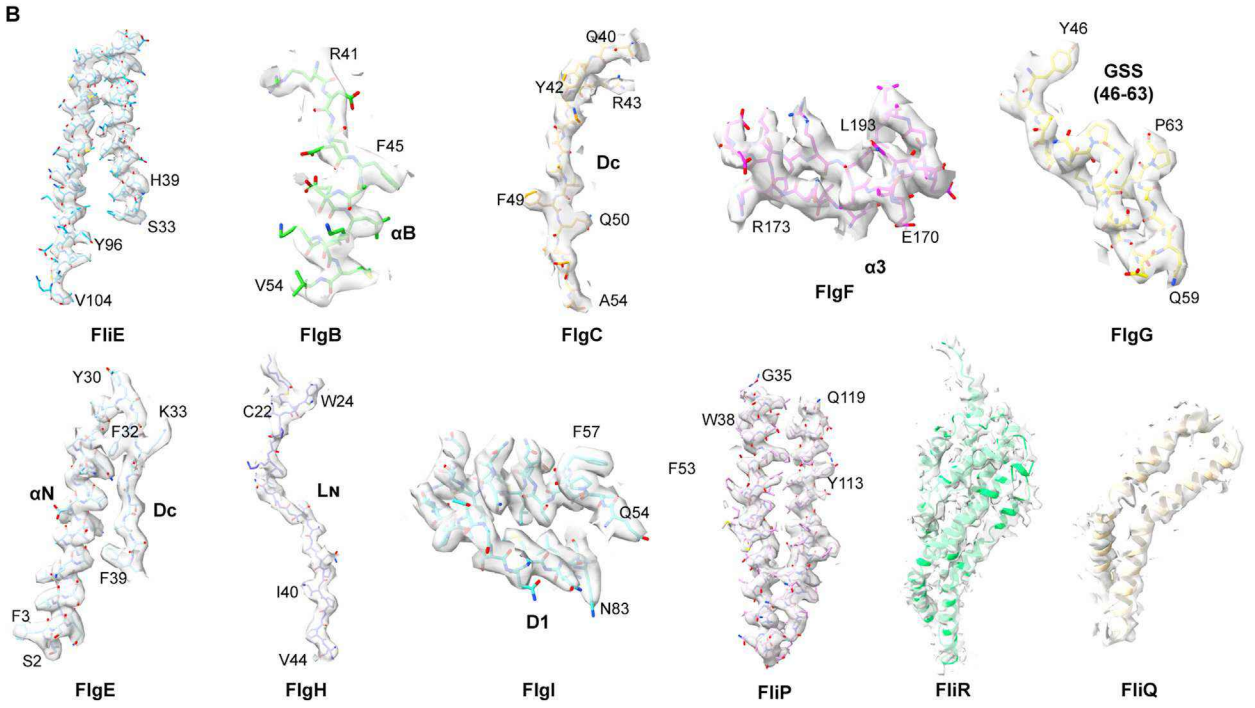

(legend on next page)

Figure S2. Local resolution maps and representative cryo-EM densities of the components of the motor-hook complex, related to Figure 1
(A) The density maps obtained in the reconstructions in Figure S1D. The map resolution is color coded for different regions. The resolution goes to 2.8 to 6.8Å.
(B) Representative density maps of FliE, FlgB, FlgC, FlgF, FlgG, FlgE, FlgH, FlgI, FliP, FliR and FliQ after local refinements. The densities of the FliE, the α_B helix of FlgB, a region in the Dc domain of FlgC, the α3 helix of FlgF, the GSS region of FlgG, the D0 domain of FlgE, the L_N loop of FlgH, the D1 domain of FlgI, the FliP N-terminal helices, FliR and FliQ are illustrated in the figure.

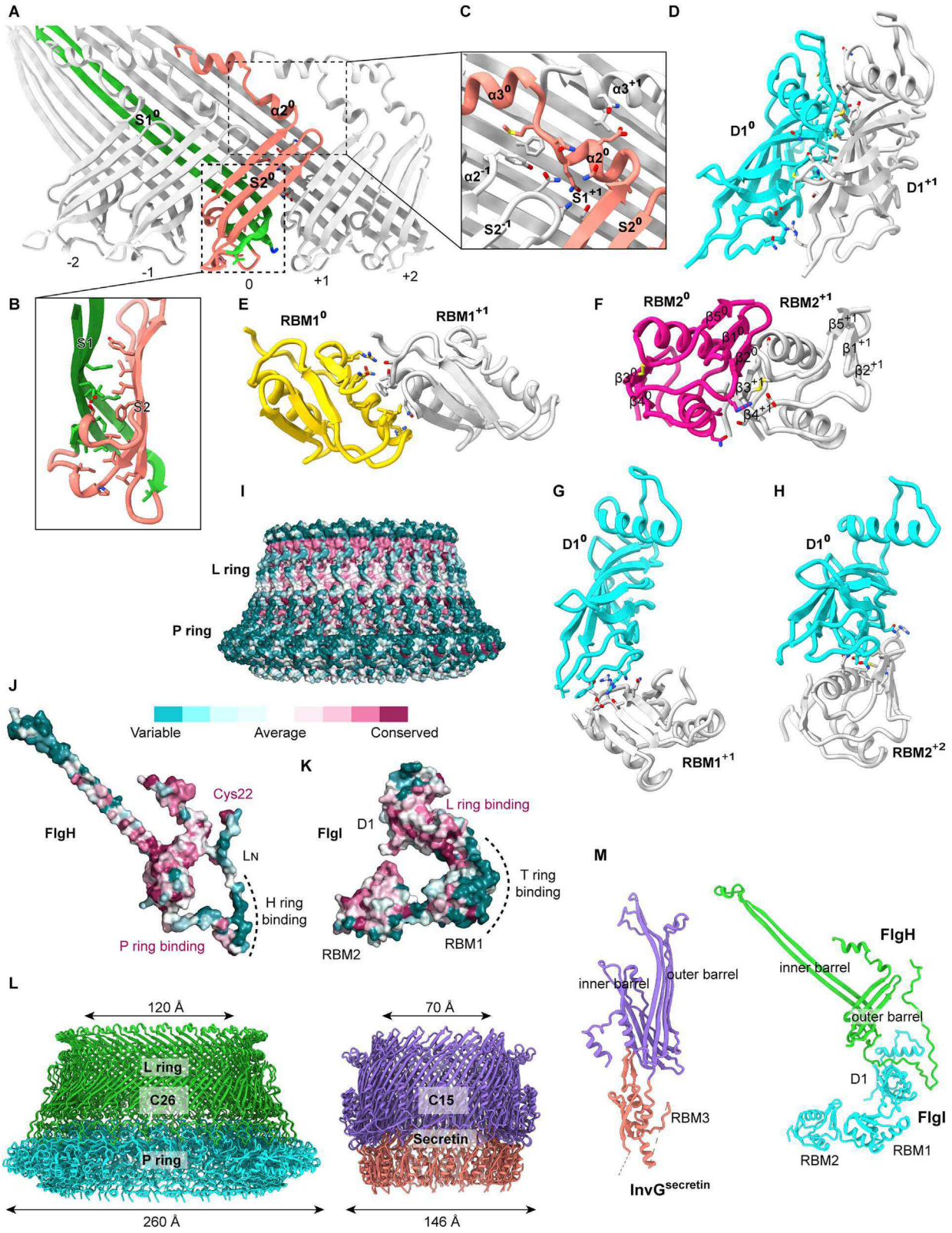

(legend on next page)

Figure S3. Intersubunit interactions and sequence conservation analyses of FlgH and FlgI in the LP ring, related to Figure 2

(A-C) S1-S2 interactions in a FlgH protomer and the interactions of the α2 and α3 helices with neighboring FlgH subunits in the L ring. The $FlgH^0$ protomer is colored as in Figure 2E. The interacting neighboring FlgH subunits are colored in gray (A). The interacting residues of the S1 and S2 β sheets in a FlgH protomer are shown as sticks (B). The interacting residues of the α2 and α3 helices are colored in salmon. The α2-interacting and α3-interacting residues in neighboring FlgH subunits are shown as sticks in gray (C). The secondary structures from different FlgH subunits are labeled with corresponding number superscripts.

(D-H) Domain-domain interactions of FlgI subunits in the three subrings of the P ring. The D1-D1 domain interactions of FlgI subunits in the inner D1 subring (D), the RBM1-RBM1 domain interactions in the outer RBM1 subring (E) and the RBM2-RBM2 domain interactions in the bottom RBM2 subring (F), the interactions of the D1 domain with adjacent RBM1 (G) and RBM2 (H) domains are shown as indicated. The intra-domain disulfide bond formed by Cys273 and Cys357 in the RBM2 domain is shown as sticks and colored in yellow (F). All interacting residues are shown as sticks. The D1, RBM1 or RBM2 domain of the adjacent FlgI subunit is labeled with corresponding number superscript.

(I)-(K) Sequence conservation analyses of FlgH and FlgI in the structure of the LP ring. The sequence conservation scores of FlgH (J) and FlgI (K) were calculated by the ConSurf server (https://consurf.tau.ac.il/). In the structure of FlgH, the residues that participate in FlgH oligomerizaiton for the L ring in the S1 and S2 sheets and the P ring-interacting residues in the L_N loop are highly conserved, whereas the residues in the N-terminal region of the L_N loop and those in the α1 helix, which form the outer surface and top edge of the L ring, respectively, are highly variable (I-J). In the structure of FlgI, the residues that mediate the FlgI oligomerization for the P ring and the interactions with the L ring are highly conserved. The residues forming the outer surface of the P ring in FlgI are highly variable (I), (K). FlgH, FlgI and the LP ring are represented as surfaces (I)-(K).

(L) Structure comparison of the LP ring with the T3SS secretin channel (PDB: 6Q15) (Hu et al., 2019). The inner and outer diameters of the LP ring and the T3SS secretin channel are labeled and indicated.

(M) Structure comparison of FlgH and FlgI with the secretin promoter ($InvG^{secretin}$) of T3SS.

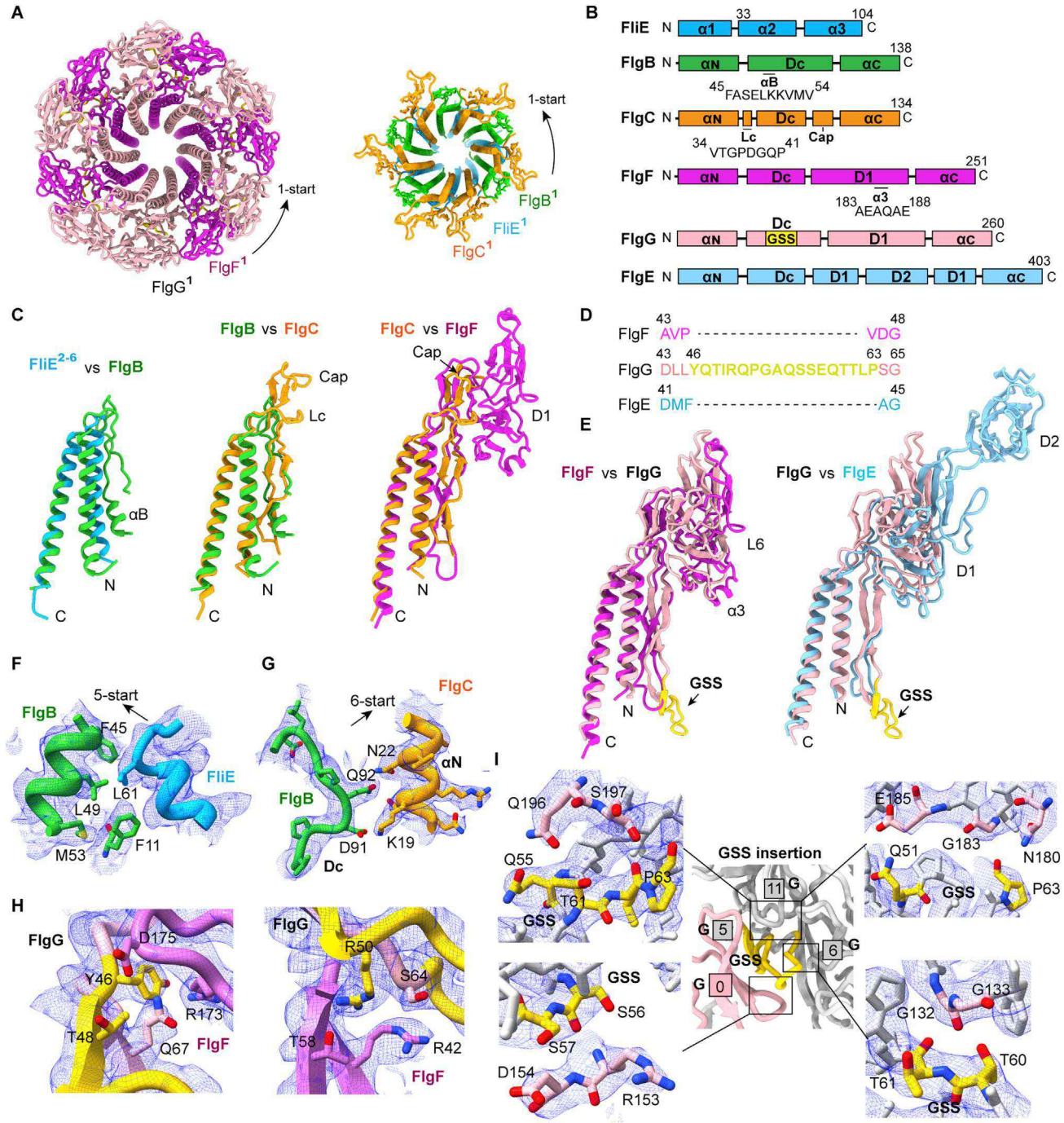

Figure S4. Structures and detailed interactions of the rod proteins, related to Figures 3 and 4

(A) Top views of the FlgF-FlgG stacking in the distal rod (left) and the stacking of the FliE, FlgB and FlgC subunits in the proximal rod (right). The FliE, FlgB, FlgC, FlgF, and FlgG subunits are colored in cyan, green, orange, purple and pink, respectively.

(B) Schematic diagrams for the domains of the rod proteins and the hook protein FlgE.

(C) Structural comparison of FliE, FlgB, FlgC and FlgF.

(D) Sequence alignment of the GSS region of FlgG with the corresponding regions of FlgF and FlgE.

(E) Structural comparison of FlgF, FlgG and FlgE.

(F) Densities of the interacting residues involved in the FliE-FlgB interactions, related to Figure 3H.

(legend continued on next page)

(G) Densities of the interacting residues involved in the FlgB-FlgC interactions, related to Figure 3J
(H) Density maps of the detailed interactions of the GSS region of FlgG with FlgF subunits, related to Figure 3L.
(I) Density maps of the detailed interactions of the GSS region with three D1 domains of the FlgG subunits at the 0-, 6- and 11-start positions, related to Figure 3N. Densities of the interacting residues are shown as blue mesh (F)-(I).

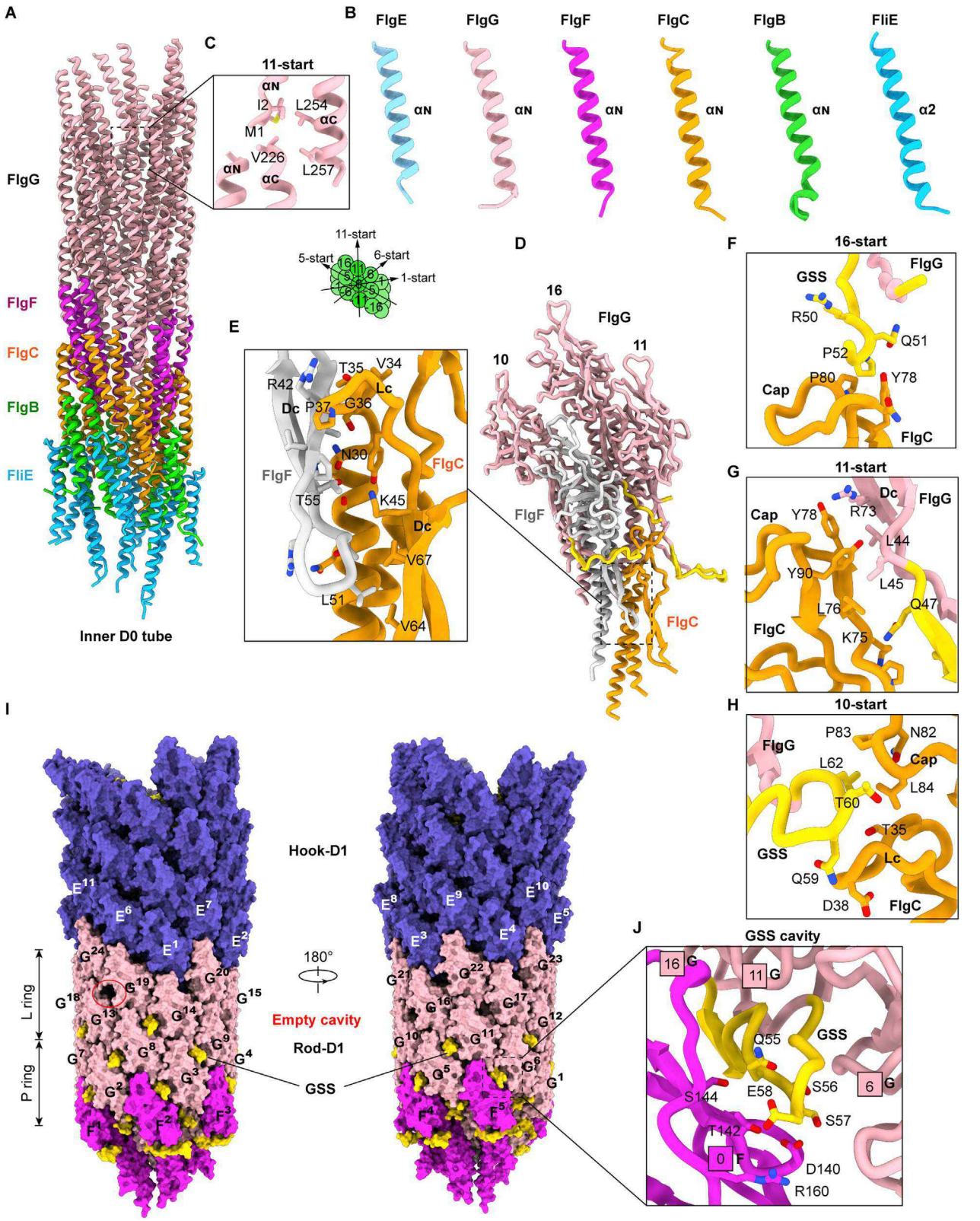

(legend on next page)

Figure S5. Interactions of the rod proteins in the rod and at the rod-hook interface, related to Figures 3 and 4

(A) The intersubunit interactions of the rod proteins in the inner D0 tube of the rod. The α2 and α3 of the FliE subunits, and the D0 domains of the FlgB, FlgC, FlgF and FlgG subunits are colored in cyan, green, orange, purple and pink, respectively.

(B) Structural comparison of the α2 helix of FliE, the α_N helices of the other rod proteins, and the α_N helix of FlgE. The α_N helices of FlgE, FlgG, FlgF, FlgC and FlgB, and the α2 helix of FliE were superimposed and then illustrated individually in the figure.

(C) The detailed head-tail interactions of the D0 domains of the FlgG subunits along the 11-start helical direction. The interacting residues are shown as sticks.

(D-H) Interactions of FlgC with FlgF and FlgG in the rod. FlgC interacts with FlgF along the 5-start helical direction. The detailed interactions of the Dc domain of FlgF with FlgC are shown in (E). FlgC interacts with three FlgG subunits along the 11-, 16- and 10-start helical directions. The detailed interactions of the cap region of FlgC with the GSS region of the FlgG subunits along the 16- and 11-start helical directions are shown in (F) and (G), respectively. The detailed interactions of the cap region of FlgC with the Dc domain of the FlgG subunits along the 10-start helical directions are shown in (H).

(I) The interactions of the distal rod with the middle tube of the hook at the rod-hook interface. The FlgF and FlgG subunits, and the D1 domains of the FlgE subunits (colored in blue) are represented in surface. The GSS regions of FlgG subunits are highlighted in yellow. The FlgF and FlgG subunits and the $FlgE^{1-11}$ subunits at the rod-hook interface are briefly labeled as F, G and E, respectively, with corresponding number superscripts.

(J) A magnified view of an interface of the FlgG GSS region with the D1 domain of FlgF. The residues Q55-E58 of the GSS region make major interactions with the FlgF D1 domain. The 6-, 11-, and 16-start helical directions are highlighted in small boxes.

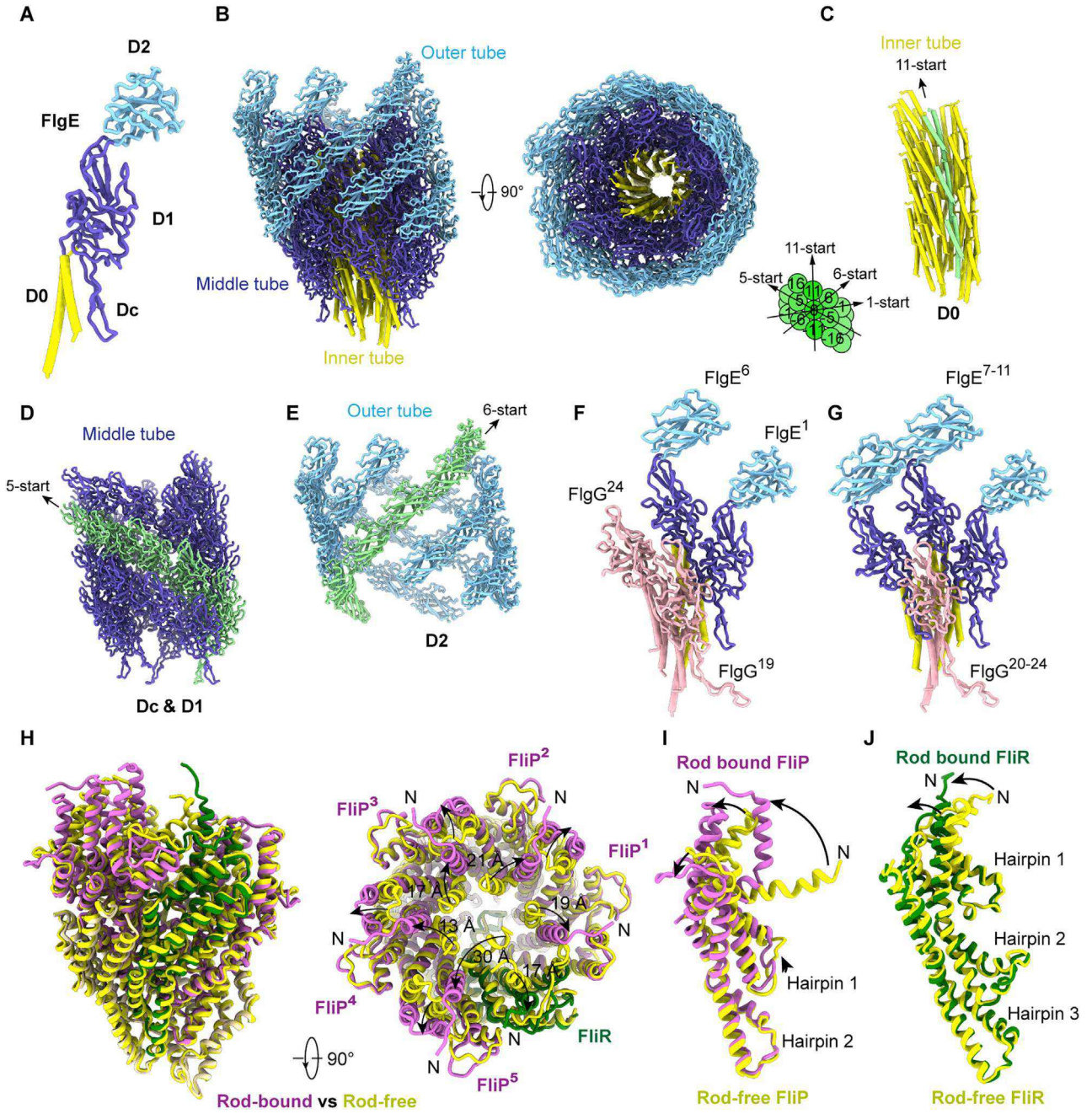

Figure S6. Structure of the hook in the motor-hook complex and conformational changes of the export apparatus upon rod binding, related to Figures 4 and 5

(A) Structure of FlgE in the motor-hook complex. The D0, D_C-D1 and D2 domains are colored in yellow, blue and light blue, respectively.

(B) Overall structure of the hook in the motor-hook complex. The inner tube (assembled by the D0 domains of FlgEs), the middle tube (assembled by the D_C and D1 domains of FlgEs) and the outer tube (assembled by the D2 domains of FlgEs) are colored in yellow, blue and light blue, respectively.

(C-E) Close-up views of the inner (C), middle (D) and outer (E) tubes of the hook. The D0 domains along the 11-start helical direction in the inner tube (C), the D1 domains along the 5-start helical direction in the middle tube (D), and the D2 domains along the 6-start helical direction are highlighted in green (E).

(F) Interactions of $FlgE^6$ with the $FlgG^{19}$, $FlgG^{24}$ and $FlgE^1$ subunits along the −11-, −6- and −5-start helical directions, respectively, at the rod-hook interface. $FlgE^6$ interacts with two FlgG subunits, $FlgG^{19}$ and $FlgG^{24}$.

(G) Interactions of the $FlgE^{7-11}$ subunits with neighboring FlgE or FlgG subunits at the rod-hook interface. Each of the $FlgE^{7-11}$ subunits only interacts with one FlgG subunit along the −11-start helical direction.

(legend continued on next page)

(H) Structural comparison of the rod-bound export apparatus in the motor-hook complex with the rod-free export apparatus (PDB: 6F2D) (Kuhlen et al., 2018). The rod-free export apparatus is colored in yellow.
(I) Structure comparison of the rod-bound FliP with the rod-free FliP (yellow, PDB: 6F2D).
(J) Structure comparison of the rod-bound FliR with the rod-free FliR subunit (yellow, PDB: 6F2D). The conformational changes of FliP and FliR are indicated with black arrows (H)-(J).

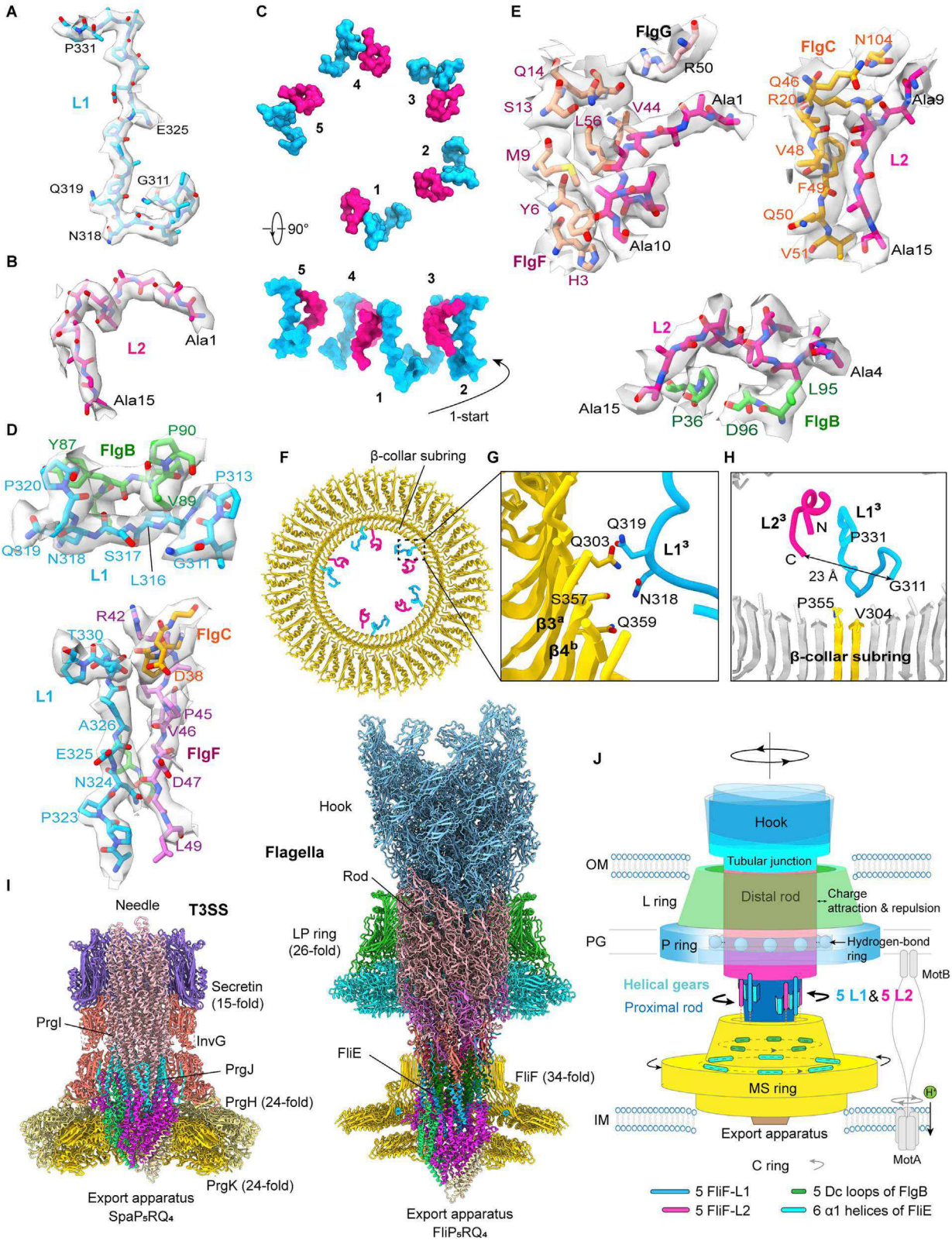

(legend on next page)

Figure S7. Structures of L1 and L2 peptides and structural comparison of the motor-hook complex with the T3SS basal body, related to Figure 7

(A-B) Representative density maps of the L1 (A) and L2 peptides (B) of the MS ring. The models of L1 and L2 are shown as sticks and labeled as indicated.

(C) Top view (upper) and side view (down) of the packing of the five pairs of the L1 and L2 peptides on the surface of the rod via the same helical parameters as those of the rod proteins.

(D) Density maps for the detailed interactions of the L1 peptide with the FlgB, FlgC and FlgF subunits, related to Figure 7E. To clearly present the densities of the interacting residues, the interface of the L1 peptide with the rod proteins is divided into two panels (upper and down).

(E) Density maps for the detailed interactions of the L2 peptide with the FlgB, FlgC, FlgF and FlgG subunits, related to Figure 7F. To clearly present the densities of the interacting residues, the interface of the L2 peptide with the rod proteins is divided into three panels (upper, middle and down). Densities of the interacting residues are colored in gray (D)-(E).

(F-G) Interactions of the L1 peptides with the β-collar ring of the MS ring. The L1 peptides interact with the β-collar subring of the MS ring (F). The interface of the $L1^3$ peptide and the β-collar ring is illustrated in (G). The $L1^3$-interacting β strands of the β-collar subring from two FliF subunits are colored in yellow and labeled as indicated. The interacting residues are shown as sticks.

(H) The distance between the N terminus of $L1^3$ and the C terminus of $L2^3$. The terminal residues of the β3 and β4 strands of the FliF subunit close to the pair of $L1^3$ and $L2^3$ are shown as sticks.

(I) Structural comparison of the flagellar motor-hook complex with the T3SS basal body (PDB: 6Q15) (Hu et al., 2019). The secretin channel, the InvG periplasmic regions, PrgH/PrgK, PrgJ and PrgI in the T3SS basal body are colored in blue, salmon, yellow, cyan and pink, respectively. The SpaP, SpaR and SpaQ subunits of the export apparatus in the T3SS basal body are colored in purple, green and wheat, respectively. The structures of the flagellar motor-hook complex and the T3SS basal body are illustrated from cross-section side views.

(J) Schematic diagram of the working model for the torque transmission of the flagellar motor. In brief, the stator MotAB conducts the proton translocation and transmits the torsional force for rotation of the C ring and MS ring. 5 pairs of the L1 and L2 peptides of the MS ring, the α1 helices of 6 FliE subunits and the Dc loop regions of 5 FlgB subunits overcome the symmetry mismatch between the MS ring and the rod and transmit the torque to the rod. The LP ring utilizes a hydrogen-bond ring as a ball bear and applies electrostatic repulsion and attraction to facilitate the high-speed rotation of the rod. The tight tubular conjunctions between the hook and the distal rod carry out torque transmission to the hook and finally induce the rotation of the filament.